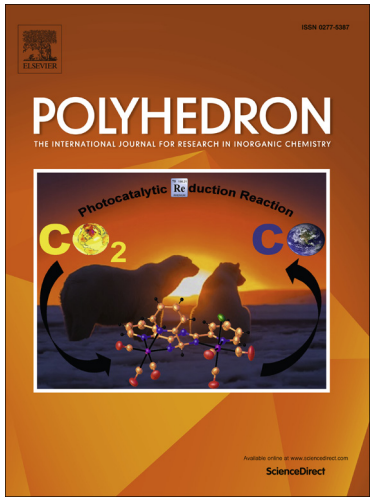

Distorted tetrahedral bis-(N,S) bidentate Schiff base complexes of Ni(II), Cu(II) and Zn(II): Synthesis, characterization and biological studies

Nanjan Nanjundan, Ramaswamy Narayanasamy, Steven Geib, Krishnaswamy Velmurugan, Raju Nandhakumar, Manickam Dakshinamoorthi Balakumaran, Pudupalayam Thangavelu Kalaichelvan

PII: S0277-5387(16)00144-3
DOI: http://dx.doi.org/10.1016/j.poly.2016.02.049
Reference: POLY 11866

To appear in: *Polyhedron*

Received Date: 4 December 2015
Accepted Date: 24 February 2016

Please cite this article as: N. Nanjundan, R. Narayanasamy, S. Geib, K. Velmurugan, R. Nandhakumar, M.D. Balakumaran, P.T. Kalaichelvan, Distorted tetrahedral bis-(N,S) bidentate Schiff base complexes of Ni(II), Cu(II) and Zn(II): Synthesis, characterization and biological studies, *Polyhedron* (2016), doi: http://dx.doi.org/10.1016/j.poly.2016.02.049

Distorted tetrahedral bis-(N,S) bidentate Schiff base complexes of Ni(II), Cu(II) and Zn(II): Synthesis, characterization and biological studies

Nanjan Nanjundan[a], Ramaswamy Narayanasamy*[a], Steven Geib[b], Krishnaswamy Velmurugan[c], Raju Nandhakumar[c], Manickam Dakshinamoorthi Balakumaran[d], Pudupalayam Thangavelu Kalaichelvan[d]

[a]*Department of Chemistry, Coimbatore Institute of Technology ,Coimbatore-641 014, India.*

[b]*Department of Chemistry, University of Pittsburgh, PA 15260 USA.*

[c]*Department of Chemistry, Karunya University, Karunya Nagar, Coimbatore - 641 114, India.*

[d]*Centre for Advanced Studies in Botany, School of Life Sciences, University of Madras, Guindy Campus, Chennai - 600 025, Tamil Nadu, India.*

*To whom correspondence should be addressed, e-mail: narayanasamycit@gmail.com

Fax: + 91-422-2575020.

Abstract

Transition metal complexes of acetophenone-S-allyldithiocarbazate **[H-(Ap-sadtc)]** of the general formula **[M-(Ap-sadtc)$_2$]** (Ni^{2+}, Cu^{2+}, Zn^{2+}) (**1-3**) were synthesized and characterized by elemental analysis, UV-Vis, FT-IR, ^{1}H NMR, ^{13}C NMR and mass spectroscopy. The molecular structures of the ligand and its complexes **1-3** were confirmed by both theoretical as well as experimental methods. The interactions of the complexes with biomolecules, such as calf thymus DNA (CT-DNA) and bovine serum albumin (BSA), were explored using absorption and emission spectral techniques. All the complexes synthesized were found to be most promising due to their large binding affinity towards different bio-macromolecules and higher K_{cat} values in catechol oxidation (3,5-DTBC) / phosphate hydrolysis (4-NPP) reactions. The *in vitro* anticancer activities using MTT and a morphological staining assay indicate that the complexes are active against the (Hela) cervical cancer cell line, which is consistent with our above mentioned hypothesis.

Keywords: Schiff base complexes, X-ray/DFT study, DNA/BSA binding activities, catalytic efficacy, *in vitro* anticancer activities.

1. Introduction

Transition metal complexes have become of increasing importance in synthetic chemistry, coordination chemistry, homogenous catalysis and biological chemistry [1]. Platinum based drugs have been found to be potentially active for their diverse clinical cancer treatment [2-6]. The dose of cisplatin that can be applied to patients is limited by its high toxicity, and the side effects of cisplatin therapy include damage to the kidney (nephrotoxicity), hearing (ototoxicity), peripheral neuropathy and neurotoxicity, nausea and vomiting. Therefore, considerable attempts are being made to replace this drug with suitable alternatives, and numerous transition metal complexes have been synthesized and tested for their cytotoxicity. In general, Schiff base metal complexes have widespread applications in electrochemistry, nanotechnology, catalysis, material science and as potential therapeutic agents. Amongst these, N,S bidentate Schiff base ligands derived from thiosemicarbazone or dithiocarbazate have attracted considerable interest. The versatile applications of dithiocarbazate ligands containing metal atoms coordinated with sulfur and nitrogen donors due to their soft-hard nature are attractive and allow them to show a structure-activity relationship (SAR) [7]. The first row transition elements play a vital role in the synthesis of several coordination complexes due their different oxidation states which facilitate their structural, stereochemical, spectroscopic and electrochemical properties. Among the various transition metals, the present study is focused on nickel, copper and zinc metal ions based on their widespread industrial and biological applications [8-11].

The transition metal ions (Ni, Cu and Zn) attached to the donor atoms of the bis(dithiocarbazate) Schiff base ligand form stable metal ion complexes. Metal-based anticancer drugs exhibit enhanced selectivity and novel modes of DNA interaction, like non-covalent interactions that mimic the mode of interaction of biomolecules. The propensity for the interaction of metal complexes with calf thymus DNA (CT-DNA) is of paramount importance to understand the mechanism using emission spectral titrations. On the other hand, the design of protein targeting metal-based anticancer agents with potential *in vitro* toxicity has gained importance recently [12,13]. Changing the ligand environment towards a specific target is one way of tuning the selectivity of a drug molecule. In another way, a change in the metal environment plays a significant role in the binding of the metal complex to a biomolecule, such as DNA or protein. Generally, nickel and copper metal ions have redox nature, which may promote the

transformation of biomolecules through an oxidation pathway [14]. In addition, the redox inactive zinc metal ion behaves in a different way [15]. Thus, these three mononuclear metal complexes have unique structural features which justify their selection for the present investigation.

Many studies have been carried out to establish a relationship between copper-mediated substrate oxidation and structural parameters, which will influence catecholase activities. Crucial factors, such as metal–metal distance, electrochemical properties, exogenous bridging ligand, ligand structure and pH of the medium, do play a major role in the catecholase activity [16-21]. Recently, it was documented that the presence of a positive charge center close to the metal center might enhance activity. Therefore, much attention has been focused on biomimetic and bioinspired catalysts of transition metal-based complexes containing hard and soft donor atoms [22,23]. Among the metal complexes, M(II) complexes with N,O and N,S-donor ligands have profound catalytic efficacy, particularly in catalyzing 3,5-DTBC to 3,5-DTBQ. Furthermore, active research on hydrolytic catalysis of phosphoric and carboxylic acid esters involving biochemical processes have gained utmost importance. The backbones of DNA, RNA and ATP macromolecules show significant biochemical behavior involving the formation or cleavage of P-O bonds [24-34]. The hydrolyses of phosphate monoester bonds in model complexes, such as 4-nitrophenyl phosphate (4-NPP), exhibit specific reactions which indicate the reactivity of metalloenzymes with DNA. When compared to other transition metals, Ni, Cu and Zn ions possess very favorable catalytic activity from the reactant and product release viewpoint [35-45].

Influenced by the above facts, it was considered worthwhile to undertake the synthesis and characterization of the ligand [H-(Ap-sadtc)] and the mononuclear complexes [Ni-(Ap-sadtc)$_2$] (**1**), [Cu-(Ap-sadtc)$_2$] (**2**) and [Zn-(Ap-sadtc)$_2$] (**3**), which confirm the presence of quite appreciable tetrahedral distortions about the metal centers. The ligand and its complexes **1**-**3** are envisaged by applying density functional theory (DFT) calculations that determine the quantum mechanical (QM) reactivity descriptors, viz. the highest occupied molecular orbital (HOMO) and lowest unoccupied molecular orbital (LUMO). A comparative study of the biomolecular interactions (DNA/BSA) of the metal complexes were conducted along with their related anti-cancer activities. The results of the present investigation confirm that the metal complexes could bind to DNA in the intercalation mode and BSA exhibiting the static quenching mechanism.

These three structurally similar complexes exhibit good catecholase and hydrolytic activities. Moreover, the cytotoxicity of the metal complexes against the HeLa cell line was assessed by an MTT assay and cell death analysis by AO/EB and DAPI staining methods.

2. Experimental

2.1. Reagents

Potassium hydroxide pellets, hydrazine hydrate, carbon-disulfide, acetophenone, nickel(II) acetate tetrahydrate, copper(II) acetate monohydrate and zinc(II) acetate dihydrate high purity reagents were purchased from Merck and used as such. Calf thymus DNA (CT-DNA) and bovine serum albumin (BSA) were obtained from Genei, Bangalore and Himedia, India respectively. Ethidium bromide (EB), 3,5-tris(hydroxymethyl) amino methane, di-*tert*-butylcatechol (3,5-DTBC), 4-nitrophenyl phosphate disodium salt hexahydrate (4-NPP) and allyl bromide were purchased from Sigma-Aldrich and used as received. All solvents were dried and used freshly, distilled unless otherwise stated. Double distilled water was used to prepare buffers.

2.2. Instrumental methods

Melting points were measured on an Electro-thermal model 9200. C, H, N and S elemental analyses of the compounds were performed on a CHNS-O model EA 2000 elemental analyzer. Electronic spectra of the ligand/complexes **1**-**3** were recorded in DMSO using a Shimadzu UV-1650 PC spectrophotometer in the 800-200 nm range. Fourier Transform Infrared spectra of the synthesized compounds were carried out with a Bruker Scientific 600 Infrared spectrophotometer in the spectral range 4000-400 cm^{-1} using KBr pellets. ^{1}H and ^{13}C NMR spectra were obtained on a Bruker High Resolution console (300.13 MHz, $CDCl_3$). Emission spectra were measured with a Jasco FP 6600 spectrofluorometer. ESI-MS spectra were recorded using an LC-MS Q-TOF micro analyzer (Shimadzu) in the SAIF, Punjab University, Chandigarh. The X-ray intensity data were measured on a Bruker Apex II CCD system equipped with a Cu IMuS micro-focus (λ = 1.54178 Å). The frames were integrated with the Bruker SAINT software package using a narrow-frame algorithm. Geometry optimization by density functional theory (DFT) method was performed using the GAUSSIAN09 (B3LYP) package. All reactions were carried out in an oxygen atmosphere. Stock solutions of complexes **1**-**3** (1.0×10^{-3} M in DMSO) were stored at 4 ^{o}C and the required concentrations were prepared for all

experiments. All the stock solutions were used after no more than four days. Solutions of the compounds were freshly prepared 1 hour prior to biochemical evaluation. Data are expressed as the mean ± standard deviation from three independent experiments.

2.3.1. Synthesis of [H-(Ap-sadtc)]

[H-(Ap-sadtc)] was synthesized according to the previously published procedure [46,47]. To an ethanolic solution (30 mL) of 5 mL (0.1 mol) hydrazine hydrate and 5.6 g (0.1 mol) KOH, carbon disulfide 6.1 mL (0.1 mol) was added dropwise in an ice bath. After 30 min, 8.6 mL (0.1 mol) of allyl bromide was added and the solution was stirred at 5 °C for 1 h. An ethanolic solution (25 mL) of acetophenone 11.7 mL (0.1 mol) was added to this mixture and heated under stirring. After 15 mins, a yellow product was separated by filtration, washed with water and vacuum dried. The product was recrystalised from hot ethanol and single crystals for X-ray structure analysis were obtained by the slow evaporation method. Yield: 75-80%. Colour: yellow. MP: 145 °C. Anal. Calc. for $C_{12}H_{14}N_2S_2$: C, 57.64; H, 5.64; N, 11.19; S, 25.61; Found: C, 57.49; H, 5.54; N, 11.06; S, 25.48%. UV-vis (DMSO), λ_{max} (nm): 368. FT-IR (ν cm^{-1}, KBr): 1596 ν(C=N); 3057 ν(N-H); 1043 ν(C=S); 982 ν(C-S); 680 ν($C\text{-}H_{Allyl}$); 1515, 1546, 1561, 1627, 1693, 1677 ν(C_{Ar}). ^{1}H NMR (300.13, MHz, $CDCl_3$, 25 °C) δ (ppm): 5.20 (m, 2H, $-CH_2$); 5.94 (m, H, -CH); 3.88 (d, H, -CH); 9.9 (s, H, -NH); 2.39 (s, 3H, $-CH_3$); 7.40-7.93 (d, 5H, C_{Ar}). ^{13}C NMR (300.13, MHz, $CDCl_3$, 25 °C) δ (ppm): 119.27 ($-CH_2$); 130.62 (-CH); 37.45 (-CH2); 200.06 (C=S); 158.19 (C=N); 15.51 (CH_3); 127.09-138.88 (C_{Ar}). ESI-MS (Calc., found, m/z): 250.38, 250.37.

2.3.2. Synthesis of complexes **1**-**3**

[Ni-(Ap-sadtc)$_2$] (**1**)

A boiling methanolic solution (20mL) of $Ni(CH_3COO)_2.4H_2O$ (0.248 g, 1 mmol) was added dropwise to a methanol solution (10 mL) of **[H-(Ap-sadtc)]** (0.5 g, 2 mmol) with an immediate colour change from yellow to brownish black. The solution was then refluxed for 1 hour. After cooling, it was filtered and the filtrate was kept at an ambient temperature for slow evaporation. After two days, the brownish-black needle-shaped diffraction quality crystals that deposited were collected by filtration, washed with small amounts of methanol and air dried. Yield: 88%. Colour: brownish black. MP: 175-178 °C. Anal. Calc. for $C_{24}H_{26}N_4NiS_4$: C, 51.71; H, 4.70; N,

10.05; S, 23.01; Found: C, 51.68; H, 4.59; N, 9.98; S, 22.89%. UV-vis (Tris-HCL buffer), λ_{max} (nm): 236, 260, 387, 479. FT-IR (ν cm^{-1}, KBr): 1532 ν(C=N); 923 ν(C-S-S); 688 ν($C\text{-}H_{Allyl}$); 1516, 1546, 1561, 1626, 1677, 1693 ν(C_{Ar}). ^{13}C NMR (300.13, MHz, $CDCl_3$, 25 °C) δ (ppm): 119.02 (-CH_2); 178.88 (C-S); 22.80 (-CH_3); 129.96-139.50 (C_{Ar}); ESI-MS (Calc., found, m/z): 557.44, 557.1.

2.3.3. [Cu-(Ap-sadtc)$_2$] (**2**)

A methanolic solution of $Cu(CH_3COO)_2.H_2O$ (0.199 g, 1 mmol) was added dropwise to a hot acetonitrile solution of **[H-(Ap-sadtc)]** (0.5 g, 2 mmol). The resulting greenish-black mixture was refluxed for 1 hour. After cooling, the clear solution was filtered and the filtrate was kept in a $CaCl_2$ desiccator in the dark. After one week, square-shaped X-ray quality crystals were filtered and washed with a small amount of petroleum ether/acetonitrile. Yield: 85%. Colour: greenish black. MP: 190-195 °C. Anal. Calc. for $C_{24}H_{26}CuN_4S_4$: C, 51.26; H, 4.66; N, 9.96; S, 22.81; Found: C, 51.07; H, 4.50; N, 9.81; S, 22.68%. UV-vis (Tris-HCL buffer), λ_{max} (nm): 238, 314, 393, 493. FT-IR (ν cm^{-1}, KBr): 1532 ν(C=N); 922 ν(C-S-S); 691 ν($C\text{-}H_{Allyl}$); 1516, 1546, 1561, 1626, 1677, 1693 ν(C_{Ar}). ESI-MS (Calcd, found, m/z): 562.3; 562.27.

2.3.4. [Zn-(Ap-sadtc)$_2$] (**3**)

An ethanolic solution of $Zn(CH_3COO)_2.2H_2O$ (0.219 g, 1 mmol) was added to a hot dichloromethane solution of [H-(Ap-sadtc)] (0.5 g, 2 mmol), then heated on a water bath for 5 minutes, filtered and kept in a refrigerator. After 15 days, X-ray quality yellow crystals were obtained, filtered and washed with a small amount of petroleum ether/ethanol. Yield: 82%. Color: Yellow. MP: 160-165 ^{o}C. Anal. Calc. for $C_{24}H_{26}N_4S_4Zn$: C, 51.10; H, 4.65; N, 9.93; S, 22.74; Found: C, 51.15; H, 4.51; N, 9.81; S, 22.60%; UV-vis (Tris-HCL buffer), λ_{max} (nm): 238, 260, 398, 497. FT-IR (ν cm^{-1}, KBr): 1533 ν(C=N); 917 ν(C-S-S); 690 ν($C\text{-}H_{Allyl}$); 1516, 1546, 1561, 1626, 1677, 1693 ν(C_{Ar}); ^{1}H NMR (300.13, MHz, $CDCl_3$, 25 °C) δ (ppm): 5.15 (m, 2H, -CH_2); 5.87 (m, H, -CH; 2.30 (m, 3H, -CH_3); 7.41-7.51 (m, 5H, C_{Ar}). ^{13}C NMR (300.13, MHz, $CDCl_3$, 25 °C) δ (ppm): 119.88 (-CH_2); 171.48 (C-S); 161.04 (C-CH_3); 21.32 (CH_3); 127.97-137.32 (C_{Ar}). ESI-MS (Calcd, found, m/z): 564.14, 564.10.

2.4. Crystal structure characterization

Single crystal X-ray data of **[H-(Ap-sadtc)]** and the three mononuclear complexes **1**-**3** were collected by a Bruker Apex II CCD diffractometer using CuK_α radiation (λ= 1.54178 Å). The linear absorption coefficients, scattering factors for the atoms and the anomalous dispersion corrections were referred from the International Tables for X-ray Crystallography. The data integration and reduction were worked out with SAINT software. The structures were solved by direct methods using SHELXTL-2014 and refined on F^2 by full-matrix least-squares using the SHELXTL-2014 program package. All the non-H atoms were treated anisotropically. The H atoms attached to carbon atoms were positioned geometrically and treated as riding atoms using SHELXL-2014 default parameters. The structures of the ligand and the three new mononuclear metal complexes **1**-**3** are shown in Fig. 1. Details of the crystallographic data, structure refinement parameters and selected bond lengths and angles are listed in Tables 1 and 2.

2.5. Computational methods

The initial geometry for the DFT calculations was based on the measured X-ray diffraction structure. All theoretical computations were done by using the Gaussian09 program package [48]. Geometry optimizations for the thione tautomeric form of the ligand and metal complexes were performed using the DFT method with Becke's three parameters hybrid exchange-correlation functional B3LYP/6-311G. Visualizations of the DFT optimized structures and the frontier molecular orbitals (HOMO and LUMO) of the ligand and complexes **1**-**3** were performed using the chemcraft program package (http://www.chemcraftprog.com). To ascertain stationary points, a further frequency test was performed. Also, a theoretical investigation of the natural charge for each atom, QM descriptors, were calculated using the same basic set.

2.6. DNA binding emission spectral studies

The interaction of the complexes with CT-DNA was investigated by dissolving the complexes **1**-**3** in a solvent mixture of 5% DMSO and 95%Tris-HCl buffer (5 mM Tris-HCl/50 mMNaCl buffer, pH = 7.2) the solutions were stored at 4 °C for further experiments and used within 4 days. Emissive titrations were performed with a fixed concentration of the metal complexes **1**-**3** (25μM) but by varying the nucleotide (CT-DNA) concentration from 0 to 10 μM. Before taking measurements, the mixture was shaken up and incubated at room temperature for 30 min. In addition, a proper wavelength with CT-DNA was fixed by the emission range and adjusted.

2.7. Competitive binding fluorescence measurements

Further, to support the competitive binding of complexes **1**-**3** to DNA via intercalation, fluorescence emission quenching experiments were performed. The fluorescence quenching experiments were carried out by adding different concentrations of complexes **1**-**3** to the EB-bound CT-DNA solution in 5% DMSO and 95% Tris-HCl buffer. The excitation (550 nm) and emission (605 nm) fluorescence intensities were recorded at room temperature. EB alone showed minimal fluorescence and the fluorescence was enhanced greatly with the gradual addition of CT-DNA until a maximum fluorescence was achieved due to the formation of an intercalative DNA-EB adduct. Addition of increasing amounts of the complexes **1**-**3** to the DNA-EB adduct quenched the fluorescence. For the emission quenching experiments, CT-DNA was pretreated with EB in a ratio [DNA]/[EB] = 10 for 30 minutes at 37 ^{o}C. The titrants were then added to this mixture of EB**-**DNA and the change in fluorescence intensity was measured.

2.8. BSA binding studies

The fluorescence spectra were recorded at an emission wavelength of 342 nm using a 4mL quartz cell on a JASCO F6500 spectrofluorometer after each addition of the quencher. Stern–Volmer and Scatchard equations and graphs were used in order to study the interaction of the quencher with BSA. Preparation of samples for fluorescence spectra: five 10 mL clean and dried sample test tubes were taken, Tris–HCl buffer 2.0 mL (pH 7.20), BSA 1.0 x 10^{-6} M and the concentrations of the complexes **1**-**3** were 10, 20, 30, 40 and 50 x 10^{-6} M for each of the five test tubes. The sixth test tube, containing only BSA solution at pH 7.2, was marked as a “control”. After mixing, the solutions were allowed to stand for 15 min for maximum binding of the complexes to BSA.

2.9. Catechol oxidase activity

In the majority of the investigations dedicated to the study of potential catecholase activity of biomimicking coordination compounds, 3,5-di-*tert*-butylcatechol(3,5-DTBC) is chosen as the model substrate because its low redox potential makes it easily oxidized to the corresponding quinone (3,5-DTBQ). Since, it prevents over oxidation, such as ring opening, and being stable, it shows a maximum emission at 435 nm in pure DMSO. Before proceeding into a detailed kinetic

study, the ability of complexes **1**-**3** were evaluated for the oxidation 3,5-DTBC to 3,5-DTBQ at room temperature in an oxygen atmospheric condition. For this purpose, 10^{-4} M DMSO solutions of these three metal complexes were treated with 10^{-2} M (100 equivalents) of 3,5-DTBC. Maintaining the complex concentration as a constant, by adding the different substrate concentrations (10-50 x 10^{-2} M), the immediate reaction progress was monitored by fluorescence spectrophotometer every 15 minutes over a reaction period of 2 hours, which was indicative for the formation of the corresponding quinone 3,5-DTBQ.

2.10. NPP hydrolysis

The rate of hydrolysis of 4-NPP was measured by monitoring the emission spectra at 485nm due to the release of the P-nitrophenolate anion. In a typical experiment, 2.0 mL of freshly prepared 4-NPP (10-50 x 10^{-2} mol dm^{-3}) in dimethyl sulfoxide (DMSO) was transferred into a cuvette in the sample compartment of the spectrometer. A similar solution was placed in a reference compartment to correct the hydrolysis in the absence of catalyst. 1.0 mL of Tris-HCl buffer(pH = 7.2) was added to the reference cuvette to bring the total volume to 3.0 mL and the cuvette was equilibrated at room temperature for 10 min. The complexes **1**-**3** (10^{-3} mol dm^{-3}) were mixed with 4-NPP separately and the emission spectra were recorded immediately and at regular time intervals of 15 mins until completion of the reaction.

2.11. Cell lines and cultural conditions

HeLa and normal Vero cell lines were cultured in RPMI-1640 medium with 10% FBS, 2mML-glutamine and 1% penicillin/streptomycin under a fully humidified atmosphere 5% CO_2 at 37 °C.

2.11.1. *In vitro* cytotoxicity by MTT assay

The effect of the synthesized compounds on the viability of the HeLa cell line was determined by an MTT (3-[4,5-dimethyl thiozole-2-yl]-2-5-diphenyl tetrazolium bromide) assay. 100µL of the cell suspensions in growth medium were plated in a 96-well microtitre plate at concentrations of 1 x 10^4 cells/well and incubated for 48 h at 37 °C in a humidified incubator. After 48 hours of incubation, the cells attained confluence; they were incubated again in the presence of various concentrations in 0.1% DMSO for 72 h at 37 °C. After removal of the sample solution, they were washed with phosphate buffered saline (pH 7.2), then 20µL of MTT (5mg/mL) was added to

each well of the plate. The plate was then incubated for 4 h at 37 °C. The solution in each well including MTT was aspirated and 100 µL of buffered DMSO was added to dissolve the formazone crystals. The plates were shaken for 5 mins and the optical density was measured on a microplate ELISA reader at 540 nm with cis-platin as a control. The cytotoxicity was obtained by comparing the absorbance between the samples and the control. The percentage inhibition was calculated as follows:

$$\% \text{ inhibition} = [\text{Abs (Control)} - \text{Abs (Test)}/\text{Abs (Control)}] \times 100$$

IC_{50} was calculated from the dose-response curve using GraphPad Prism 6 software.

2.11.2. Apoptotic assays by fluorescence microscopy

HeLa cells were seeded onto chamber slides in six-well plates at a density of 1 x 10^6 cells per well and incubated for 24 h. The cells were cultured in RPMI 1640 supplemented with 10% fetal bovine serum (FBS) and incubated at 37 °C in 5% CO_2. The medium was removed and replaced with a medium (final DMSO concentration, 0.05% v/v) containing the complexes (50 µM) for 24 h. The medium was removed again and the cells were washed with ice-cold phosphate buffer saline (PBS) and fixed with formalin (4%, w/v). Cell nuclei were counterstained with acridine orange (AO) and ethidium bromide (EB) (AO: 100 mg mL^{-1}, EB: 100 mg mL^{-1}) for 10 min. For DAPI staining, the treated cells were fixed with 80% ethanol at room temperature for 30 min. The fixative was removed and the cells were washed with PBS 3 times, and then incubated with DAPI (1 µg mL^{-1}) for 45 min at room temperature in the dark. Both techniques were used to distinguish viable cells, early apoptotic cells with blebbing and necrotic cells. Acridine orange intercalates into DNA and gives a green fluorescence and thus the viable cells appear with a green nucleus, while early apoptotic cells have condensed or fragmented nuclei. EB is taken up only by the non-viable cells, giving a bright orange nucleus of the dead cells overwhelming the acridine orange stain. DAPI dye is effective for fixed-cell staining and quantification of DNA content. HeLa cells were mounted on a slide and the images were observed under a fluorescent microscope in a green/blue filter on excitation at 350 nm and emission at 460 nm. The cells were observed and imaged with a fluorescence microscope (Nikon, Yokohama, Japan).

3. Results and discussion

3.1. Synthesis and characterization

The three novel mononuclear complexes **1**-**3**, formed in a high yield of up to 80% from a mixture of **[H-(Ap-sadtc)]** and the metal(II) acetate in a 2:1 molar ratio, are shown in Scheme 1. The complexes are pure, crystalline in nature and completely soluble in ethanol, methanol, acetonitrile, chloroform, dichloromethane, DMF and DMSO, but are insoluble in hexane, petroleum ether and diethyl ether. The complexes were characterized by elemental analysis, UV-Vis, infrared, ^{1}H NMR, ^{13}C NMR and mass spectroscopy, and by single crystal X-ray diffraction studies.

3.1.1. Infrared spectra

The FTIR spectrum of the ligand did not show any band at 2570 cm^{-1} (-SH), which indicates a solid state thione form. Two strong bands appeared for the ligand at 3057 (-NH) and 1043 (C=S) cm^{-1}, which were absent after complexation indicating that these two bands disappeared due to deprotonation of the ligand and chelation of the thiolate sulfur atom. It suggests that the thione form has been converted into the thiolate form, so that complexation can occur (Scheme 2) [49,50]. A strong vibration observed at 1596 cm^{-1} for the ligand, corresponding to the C=N band, was shifted to 1532-1533 cm^{-1} in the metal complexes due to the interaction of the azomethine nitrogen atom during bonding [51,52]. The investigated and calculated frequencies of the dithiocarbazate ligand and its complexes **1-3** are given in Table S1.

3.1.2. Electronic spectra

The electronic spectral absorption of **[H-(Ap-sadtc)]** in DMSO solution at 368 nm confirms an intra-ligand transition, which is shown in Fig. S1. The ligand exhibits an n→π* transition, which is due to coordination between the nitrogen atom and dithiocarbazate moieties. The spectra of complexes **1-3** were recorded in Tris-HCl buffer and bands appeared at 236, 260, 238 and 314 nm due to a strong absorption of azomethine nitrogen atom, as shown in Figs. S2-S4. Also, LMCT broad bands appeared at 389, 393 and 398 nm for the respective complexes **1-3**, which were mainly due to an S→M(II) charge transfer. All the complexes were expected to show the transitions $A_1g \rightarrow {}^1A_2g$, $^1A_1g \rightarrow {}^1B_1g$ and $^1A_1g \rightarrow {}^1Eg$ in the visible region, but the prepared complexes showed only a single (d-d) band at 479, 493 and 497 nm, respectively for the $^1A_1g \rightarrow {}^1Eg$ transition as the presence of sulfur covered the other bands.

3.1.3. ^{1}H NMR spectra

The thione and thiol forms of the Schiff base may also exist as either the *E* or *Z* conformational isomer, or as a mixture of both isomers in solution. However, the X-ray crystallographic structural determination of the ligand shows that in the solid state, it exists solely as the thione form. The ^{1}H NMR spectrum of the ligand in $CDCl_3$ exhibits the thione form, as indicated by the –NH resonance at 9.9 ppm, showing that in solution, it exists only as the Z isomer [53-55]. However, the thiol form may also exist in a $CDCl_3$ solution of **[H-(Ap-sadtc)]**, the ^{1}H NMR spectrum displaying a sharp signal for -SH at 4 ppm. The methylene proton of the ligand and complex **3**, appearing at 3.88 and 3.72 ppm respectively, indicates that the allyl sulfur atom is not involved in coordination. The **-**CH_2 and **-**CH protons in the allyl group show multiple peaks at 5.94-5.96 and 5.17-5.20 ppm, respectively. The aromatic protons appear as doublets within the range 7.40–7.93 ppm for [**H-(Ap-sadtc)]** and similar signal peaks are observed for the metal complexes. The **-**NH and –SH peaks in the ^{1}H NMR spectrum of the ligand disappeared upon complexation, which confirms the fact that the N and S atoms are involved in the formation of the metal complexes.

3.1.4. ^{13}C NMR spectra

The ^{13}C NMR spectra of **[H-(Ap-sadtc)]** showed signals at 200.06 and 158.19 ppm, which are attributed to the C=S and C=N groups, respectively. However, in the formation of the metal complexes **1** and **3**, the C=S group experienced a downfield shift at 171.48 and 178.88 ppm, and the C=N group an upfield shift at 161.04 and 173.94 ppm. These considerable shifts with respect to **[H-(Ap-sadtc)]** indicate the involvement of thione sulfur and azomethine nitrogen atoms in coordination. In addition, C-S carbon atom in **[H-(Ap-sadtc)]** and complexes **1** and **3** showed signals at 37.45, 38.58 and 35.59 ppm, respectively. The peaks due to the presence of aromatic carbons and the methyl group in the ligand and complexes **1** and appeared in the ranges 125.09–139.50 and 15.5-22.80 ppm respectively.

3.1.5. Crystal structure description of **[H-(Ap-sadtc)]**

A suitable single crystal was grown from the required amount of hot ethanol by the slow evaporation method over a time period of one week. A specimen of $C_{12}H_{14}N_2S_2$ of approximate dimensions 0.020 x 0.120 x 0.140 mm was used for the X-ray crystallographic analysis. The

final cell constants were based upon the refinement of XYZ-centroids of reflections above 20 σ(I). The calculated minimum and maximum transmission coefficients (based on crystal size) were 0.6370 and 0.9330. The final anisotropic full-matrix least-square refinement on F^2 showed that **[H-(Ap-sadtc)]** crystallized in the space group P-1 in the triclinic crystal system. The crystal structure of the ligand also confirms that it crystallizes as the thione tautomeric form, as previously predicted by spectroscopic techniques; with the thione sulfur and azomethine nitrogen atoms in this conformation, the ligand acts as an N,S binding agent. The C=S bond length (1.667 Å) indicates that is a double bond and the C-N bond (1.294 Å) is intermediate between a single and a double bond, indicating electron delocalization in the N-C-S thioamide group. The N–N bond distance varied from 1.376(4) to 1.4186(19), 1.396(3) and 1.403(2) Å in the Schiff base to the complexes, showing that the bond was shorter than a single bond and also indicating significant π-delocalization of the dithiocarbazate occurred in the C-N-N-C moiety. However, the rotation of the S-C-S fragment by 180° about the C-N bond orients the donor atom in the correct position for bidentate coordination.

3.1.6. Crystal structure description of the metal complexes **1-3**

X-ray quality single crystals were isolated from the mother liquors by the slow evaporation method. Specimens of $C_{24}H_{26}NiN_4S_4$, and $C_{24}H_{26}CuN_4S_4$, of approximate dimensions 0.080 x 0.090 x 0.170 and 0.120 x 0.140 x 0.160 mm were used for the X-ray crystallographic analysis. The ORTEP view of complexes **1-3** at the 25% probability level with the atom numbering scheme is shown in Fig 1. The calculated minimum and maximum transmission coefficients of the nickel and copper complexes (based on crystal size) were 0.5360, 0.5530 and 0.7300, 0.6330. The non-hydrogen atoms were refined anisotropically by applying the full-matrix least-square method on F^2. The centrosymmetric Ni(II) and Zn(II) complexes crystallized in the monoclinic space group $P_{121/n1}$, whereas the Cu(II) complex crystallized in the orthorhombic space group P_{21212}, in which the two ligands were symmetrically related to each other and had the same bond angles and distances. The central metal ion was bis-chelated by the bidentate ligand through the azomethine nitrogen (N2) and thiolate sulfur (S2) atoms.

The conjugate system of the ligand was influenced by coordination with the metals, as shown by the N1–N2 bond distance of ligand (1.376(4) Å), with a slight lengthening of the analogous bond in the complexes (1.4186(19), 1.396(3) and 1.403(2) Å). In addition, the azomethine C9–N2

bond in the nickel complex was found to be 1.282(2) Å, and the C1-N2 bonds in the copper and zinc complexes were found to be 1.287(3) and 1.285(3) Å, which are slightly shorter than in the ligand (1.343(5) Å), clearly indicating that the complexation involves deprotonation at the N1 atom. The C4-S2 bond is strongly affected in the nickel (1.7397(18) and 1.7420(17) Å) copper (1.739(2) Å) and zinc complexes (1.741(2) and 1.737(2) Å), being longer than the analogous bond in the Schiff base (1.667(3) Å). So, the C4-S2 bond involved in complexation is a single bond. The Ni–S (2.1548(5), 2.1583(5) Å), Cu-S (2.2362(7), 2.2363(7) Å), Zn-S (2.2814(5), 2.2817(5) and Ni–N (1.9320(13), 1.9254(12) Å), Cu-N (2.0011(18) Å), Zn-N (2.0546(15), 2.0674(15) Å bond lengths are similar to in the bis-chelated four coordinate mononuclear complexes **1**-**3**. The Ni(II), Cu(II) and Zn(II) central ions have bite angles of 100.91(5), 101.62(11) and 108.48(6)° for N3-M-N1, while the S3-M-S1 bond angles are 90.97(18), 101.98(4) and 115.13(2)° respectively. The geometrical parameters suggest that none of the complexes show an ideal tetrahedral geometry due to the restricted bite angles of the chelating dithiocarbazate ligands. The metal ion occupies a position on a twofold axis and adopts a distorted tetrahedral geometry. From the above facts, the geometry of complex **1** is more distorted than complexes **2** and **3**.

3.1.7. DFT calculations

The density functional theory calculations were carried out in the gas phase to optimize the structure of **[H-(Ap-sadtc)]** and its metal complexes **1**-**3**, using coordinates of the crystal structure from the CIF file. The optimized geometries of **[H-(Ap-sadtc)]** and the mononuclear complexes **1**-**3** are depicted in Fig 2. Selected bond lengths and bond angles of both the ligand and the complexes are given in Table 2. The calculated values are in good agreement with the crystallographic data in all cases. The distance for the C=S bond (1.706 Å) in the ligand is lengthened in the complexes to 1.739, 1.740, 1.805, 1.758, 1.789, and 1.779 Å, suggesting that the sulfur atom coordinates with the metal complexes. Further, the C-N bond lengths varied from the ligand to the complexes, indicating that deprotonation occurs on complex formation. The optimized structures were used in the DFT calculations of vibrational frequencies. The predicted FT-IR spectra using the B3LYP/6-311G level were correlated with an optimal scaling factor of 0.9613 [56]. The calculated FT-IR spectra present a strong correlation and are in good agreement with the experimental data [57]. The frontier molecular orbitals play an important role in the

electric and optical properties, as well as in UV-Vis spectra. The energies of the HOMO and LUMO orbitals and their orbital energy gap were calculated using the DFT method and pictorial illustrations of these frontier orbitals for the compounds are shown in Fig 2.

The highest occupied molecular orbital (HOMO) represents the outermost orbital filled by electrons and behaves as an electron donor, while the lowest unoccupied molecular orbital (LUMO) is the first empty innermost orbital unfilled by electrons and behaves as an electron acceptor. These orbitals are also called the frontier molecule orbitals (FMOs). Positive and negative regions are shown by red and blue colours, respectively. In the ligand, almost all of the molecules is localized in the HOMO and LUMO, except the allyl (–CH2-CH=CH2) moiety. The energy gap between the HOMO and LUMO characterizes the chemical stability of the molecule. The energy gaps in the case of the title ligand and compounds **1**-**3** are found to be 4.08, 1.48, 0.75 and 2.42 eV, respectively. Since, a lower energy gap implies more interaction and less stability, complex **2** has a higher chemical activity than the other compounds. This observation suggests that the photo-excitation of the complexes could result in facile electronic transitions from the HOMO, centered on the dithiocarbazate moiety, to the LUMO, spread over the M(II) ion and the N, S atoms. It can also explain the remarkable photo-cytotoxicity of the dithiocarbazate complexes. Additionally, a variety of quantum mechanical (QM) reactivity descriptors, like the electronic chemical potential (μ) chemical hardness (η) and electrophilicity ($\mathcal{G}$) were calculated with the help of the following equations:

$$\eta = (I - A)/\ 2$$

$$\mu = -\ (I + A)/2$$

$$\mathcal{G} = \mu^2 /2\ \eta$$

where $I = -\ E_{HOMO}$, $A = -\ E_{LUMO}$.

The calculated QM reactivity descriptors in Table 3 also determine the binding strength trends of the complexes. The chemical hardness is quite useful to rationalize the relative stability and reactivity of chemical species. Hard species, having a large HOMO–LUMO gap, will be more stable and less reactive than soft species, having small HOMO–LUMO gap; however, a smaller HOMO–LUMO gap requires less excitation energy and so the absorption bands of molecules are shifted towards the visible region. This suggests that the bonding of the metal(II) ion modifies the charge distribution of the π-electrons of the free ligand. This lower energy gap implies that the delocalization of π-electrons from the metal complexes will result in good non-linear optical

properties in the order **2** > **1** > **3** > **L**. The natural charge analysis indicates electrovalent bonding between the ligand and the corresponding metal complexes as listed in Table S2. The negative charge of the ligand is mainly localized on the S1, N1 and N2 atoms. Upon coordination of S1 to the metal center, the electron cloud of the C=S bond is displaced towards the S atom, which is partially compensated by electron displacement. The calculated charges on the metals were 1.1434, 1.0069 and 1.5728, comparably lower than the formal charge of +2 for the electronic configurations of complexes **1**, **2** (d^8) and **3** (d^{10}). This confirms electron transmission of the donor atoms toward the central metal.

3.2. CT-DNA binding studies

3.2.1. Fluorescence emission spectra

The binding studies of small molecules with calf thymus DNA were carried out by using fluorescence emission spectroscopy. It is well known that any antitumor drug relies on its binding character, binding mode, selectivity toward specific DNA base pairs and kinetic procedure followed during its reaction with DNA. An important class of compounds for cancer chemotherapy involves non-covalent interactions between CT-DNA and the metal complexes, such as intercalation, groove binding and electrostatic binding [81-84]. Through strong stacking, non-covalent intercalations usually result in hypochromism/hyperchromism, with or without blue/red shifts in the fluorescence emission spectra.

In the presence of increasing amounts of CT-DNA (0-10μM) at a constant metal complex concentration (25μm), the emission spectral technique was used to determine the intrinsic binding constant (k_b). The interactions of complexes **1**-**3** with DNA have shown that for the emission wavelength region of 412-429 nm, the intensity of the bands decreased from their original intensities, based on DNA binding enhancement. It suggests that the metal complexes are electron-acceptors and the DNA molecule is an electron-donor. All three metal complexes show hypochromism of 27.3, 58.1 and 41%, and a small blue shift, which may be observed when the DNA duplex is stabilized. A blue shift may also be attributed to improper coupling (due to conformational changes) of the π* orbital of the intercalated ligand with the π orbital of the base pairs. The intrinsic binding constant (K_b) has been determined using the following Scatchard equation [58]:

$$C_F = C_T [(I/I_0 - P)/1 - P]$$

where C_T and C_F are the concentrations of the probe metal complex (25μm) and the free probe, I_0 and I are the emission intensities in the absence and in the presence of DNA, respectively. The value of P is obtained from a plot of I/I_0 *versus* $1/[DNA]$, such that the limiting emission yield is given by the y-intercept. The amount of bound probe (C_B) at any concentration is equal to $C_T - C_F$. The slopes of the obtained Scatchard plots of r/C_F versus r for the tested compounds with an increasing concentration of CT-DNA (Fig. 3) gives the intrinsic binding constant (K_b) values, as listed in Table 4.

This observation suggests strong intercalation of the complexes to DNA, with complex **2** having a comparatively higher intercalation than complexes **1** and **3**, also being higher than the observed values reported earlier [59]. The presence of transition metal ions in the complexes also accounts for the higher binding extent of the complexes with CT-DNA. It has been reported earlier that a transition metal complex ultimately leads to an effective binding with the helical structure of DNA and exposes the embedded base pairs to the helix exterior via normal intercalation [60]. From the results of the binding constants, it is concluded that the complexes **1**-**3** have a strong binding affinity with CT-DNA [61].

3.2.2. EB-DNA displacement study

Ethidium bromide (EB) is a fluorescent dye and also a typical indicator of intercalation, since upon the formation of soluble complexes with nucleic acids, EB emits intense fluorescence in the presence of CT DNA due to intercalation of its aromatic ring between adjacent base pairs on the double helix. The changes observed in the spectra of EB upon its binding to CT-DNA are often used for the interaction study between DNA and other compounds, such as metal complexes. Before any measurements were taken, the mixture was shaken up and recorded. The fluorescence spectra of DNA bound EB were obtained at excitation and the emission wavelengths of 541 and 605 nm, respectively.

The quenching is due to the reduction of the number of binding sites on DNA that are available to EB. The fluorescence emission intensity of the DNA–EB system in the absence and presence of compounds added to DNA pre-treated with EB causes an appreciable reduction in the emission intensity with increasing complex concentrations. This indicates that complexes **1**-**3** can compete with EB, binding stronger to DNA. Furthermore, the quenching data were analyzed

according to the Stern–Volmer equation and K_{sv} values were obtained from the slope of the plot of I_0/I versus [Q]. The quenching plots illustrate that the quenching of EB bound to CT-DNA by complexes **1**-**3** are in good agreement with the linear Stern–Volmer equation. The K_{app} values were measured from the extent of reduction of the EB emission intensity by the complexes. The apparent binding constant values were obtained for the compounds using the following equation [62-64]:

$$K_{EB\ x}\,[EB] = K_{app}\,[M_{50\%}]$$

where $K_{EB} = 1.0 \times 10^{-7}\ M^{-1}$ is the DNA binding constant of EB, [EB] is the concentration of EB (7.5μM) and $[M_{50\%}]$ is the concentration of the compound used to obtain a 50% reduction in fluorescence intensity of DNA pretreated with EB. The Stern–Volmer constant K_{app} values of the complexes are consistent with the emission titration results. On the basis of spectroscopic studies, it is concluded that complexes **1**-**3** bind to CT-DNA in an intercalative mode and complex **2** binds to CT-DNA more strongly than the other two complexes.

3.3. BSA interaction studies

3.3.1. Fluorescence quenching study

The binding affinity of complexes **1**-**3** with BSA were examined by the fluorescence spectral technique. BSA has a strong fluorescence emission band around 342 nm, fixing the excitation wavelength at 290 nm, and the fluorescence intensity of BSA was quenched drastically when the concentrations of the complexes **1**-**3** were increased. Generally, the fluorescence quenching can be illustrated by the well-known Stern–Volmer equation [65]:

$$F_0/F = 1 + K_{SV}\,[Q] = 1 + K_q\,\tau_o\,[Q]$$

where F_0 and F are the fluorescence intensities of BSA in the absence and presence of the complexes, respectively, K_{SV} is the linear Stern–Volmer quenching constant, kq is the quenching rate constant of the biomolecule, τ_o is the average fluorescence lifetime (10^{-8} S) [66] of BSA without the quencher and [Q] is the concentration of the quenching complex. The value of K_{sv} is obtained from the slope of a linear plot of F_0/F vs [Q]. Different mechanisms occur during quenching, which are usually classified as dynamic quenching and static quenching, in which the

transient existence of an exited state of the fluorophore and the quencher is referred to as a dynamic quenching process, while static quenching is due to the formation of a ground-state complex between the fluorophore and the quencher. In both cases, the fluorescence intensity is mainly related to the concentration of the quencher. Therefore, the quenched fluorophore can serve as an indicator for the quenching agent. This linear Stern–Volmer plot indicates that more than one process contributes to the overall quenching of BSA. It has been reported in many cases that the fluorophores can be quenched by both collision (dynamic quenching) and by complex formation with the same quencher (static quenching). This complex formation is facilitated through hydrogen bonding and hydrophobic interactions. The quenching constant K_q of the complexes **1**-**3** follows the order: **2 > 1 > 3**, which is in good agreement with the trend in the DNA binding affinities. The maximum possible value for dynamic quenching is (2.0×10^{10} L mol^{-1} S^{-1}), which is comparably lower than the quenching constant of the complexes **1**-**3**. The Stern–Volmer plots show that the high quenching constant values of 10^{13}-10^{14} dm^3 mol^{-1} s^{-1} indicate that strong ground state complex formation contributes significantly to the overall quenching of fluorescence intensity of BSA [67].

3.3.2. Determination of binding parameters and binding number

Fluorescence quenching is often a result of energy transfer from a donor (Trp) to an acceptor (metal complex). However, in all the systems and combinations studied, the quenching of Trp fluorescence is static and Forster's long-range energy transfer is not taking place. When a static quenching interaction occurs, if it is assumed that the complex binds independently to a set of equivalent binding sites in BSA, the binding parameters can be determined according to the Scatchard equation [68,69]:

$$\log (F_0\text{-}F/F) = \log K'_b + n \log[Q]$$

where K'_b is the binding constant for the binding of the complex with BSA and *n* is the number of binding sites per BSA molecule. This gives a straight line in the plots of $\log(F_0\text{-}F/F)$ vs log[Q], as shown in Fig. 6.

The values of n indicate the existence of a single binding site in BSA for complexes **1-3**. The observed values of K_q, K_{bin} and 'n' indicate a strong interaction between the BSA protein and the complexes, and the values follow the order: **2 > 1 > 3**.

3.4.1. Kinetic studies for catechol oxidase activity

Detailed reactivity and kinetic studies of complexes **1**-**3** were performed in dimethyl sulfoxide (DMSO) because of their good solubility along with that of the substrate 3,5-DTBC and its product 3,5-DTBQ, as depicted in Scheme 3.

All the complexes show efficient catecholase activity at (pH 7.2) because of the de-protonation of 3,5-DTBC and subsequent binding to the metal centre before its oxidation. Upon addition of 3,5-DTBC to the metal complexes, spectral studies were carried out which showed an immediately increment of the emission bands at 435 nm, proving the oxidation of catechol to quinone (see Fig. 7). The kinetic studies used the method of initial rate by monitoring the growth of the quinone band. The oxidation rates and various kinetic parameters were determined by 10^{-4} M solutions of the complexes with different concentrations of 3,5-DTBC under aerobic conditions. In all cases, a first order kinetic dependence was observed at low concentrations of 3,5-DTBC, whereas at higher concentrations, saturation kinetics were recorded, as shown in Figs. S15-S17. The observed data were analyzed on the basis of the Michaelis-Menten approach for the enzymatic kinetic model, which seemed to be appropriate. The values of the Michaelis binding constant (K_M), maximum velocity (V_{max}) and the rate constant (K_{cat}) for the dissociation substrates were calculated for the complexes from graphs of 1/V versus 1/[S] (Fig. 7), known as the Lineweaver-Burk (double reciprocal) graph, using the equation and the kinetic parameters as listed in Table 6.

$$1/V = \{ K_M/ V_{max}\}\{1/[S]\} + 1/ V_{max}$$

Among the three mononuclear complexes reported herein, the highest catecholase activity is observed for complex **2**. If the reduction potential is too negative, the complex shows decreased catalytic activity due to more difficulty in reduction to copper(I), a more positive reduction potential of the complex gives higher catalytic activity. The donor atom on the dithiocarbazate moiety may also help to facilitate the substrate-catalyst interaction by forming a positive channel, showing better catalytic activity [70].

On account of the proposed mechanistic steps of the catecholase oxidase activity of M(II) complexes, a plausible mechanistic pathway is suggested, as depicted in Scheme 4. Upon addition of 3,5-DTBC to the metal complexes **1**-**3**, immediately the catechol molecule

coordinates to the complexes and forms an intermediate substrate-complex adduct **1a**. This result indicates a change in coordination environment of the M(II) centre from tetra to penta-coordinate [71], which may favor electron transfer and equilibration between M(II)-(3,5-DTBC) and the semiquinone intermediate M(I)-(3,5-DTBQ) (**1b**, **1c**). Its subsequent reaction with dioxygen may also result in electron reduction, leading to the oxidation of the M(I) ion and release the quinone molecule along with hydrogen peroxide as a byproduct, **1d** [72-75]. After the quinone molecule is released, the catalyst is regenerated and the catalytic cycle continues [76].

3.4.2. Kinetics of NPP hydrolysis

The hydrolytic reaction in enzyme-catalysis involves metal ions that are assumed to activate a water molecule, which forms a hydroxyl group as a nucleophile in the reaction system [77]. The M(II)-bound OH^- then acts as a nucleophile to attack the phosphate atom of 4-NPP ester, which leads to hydrolysis (Fig. 8), shown by emission increases at 485 nm due to the formation of 4-nitrophenolate ions over time (Scheme 5). Since, the catalyst concentration was essentially constant during measurements, the initial first order rates were measured at different concentrations of the substrate at pH 7.2 and room temperature. The initial rates obtained for a range of 4-NPP concentrations were fitted to the Michaelis-Menten equation (Figs. S18-S20) and linearized by means of the Lineweaver–Burk method, *i.e.* 1/rate vs. 1/[4-NPP] by changing the concentration of the substrate (Fig. 8). The kinetic parameters of K_M, V_{max} and the catalytic constant K_{cat} values are summarized in Table 7. Hydrolysis of 4-nitrophenylphosphate by the Cu(II), Ni(II) and Zn(II) complexes show that the Cu(II) complex has a higher catalytic activity than the Ni(II) and Zn(II) complexes, similar to earlier reports [78,79]. All the complexes have shown better efficacy than catecholase activity.

3.5.1. *In vitro* anticancer activity evaluation by an MTT assay

In the present study, the antitumor efficacy of complexes **1**–**3** was assayed by determining the viability of HeLa cells using an MTT assay and cis-platin was used as a positive control to assess the cytotoxicity of the tested mononuclear complexes. The results were analyzed by means of cell inhibition, expressed as IC_{50} values which are listed in Table 8. It is notable that complex **2** possesses the most potent inhibitory effect against the HeLa cell line. The IC_{50} value is well

known for the anticancer drug cisplatin, as shown in Fig. 9. The results of the MTT assay in Table 8 shows that complexes **1-3** inhibit the growth of cells in a concentration dependent manner. A low IC_{50} value implies cytotoxicity at low drug concentrations. The significant inhibitory activity of the complexes and their binding affinity to CT-DNA/BSA clearly indicates that the incorporation of the complexes has a marked effect on the cytotoxicity. In addition, an *in vitro* cytotoxicity assay conducted on a HeLa cancer cell line versus normal vero cell line has demonstrated that complexes **1**-**3** show profound anticancer activity.

3.5.2. AO-EB/DAPI staining assay

Cell apoptosis is an autonomic ordered programmed cell death in order to maintain homeostasis, which is controlled by serial genes. The morphological changes of HeLa cells have been observed under a light microscope. The design of chemotherapeutic drugs, in order to understand the complexities of apoptosis evolved by cancer cells and the development of strategies to selectively induce apoptosis in cancer cells, have turned into a unique target in cancer drug development [80]. The morphological changes induced by complexes **1**-**3** were evaluated using AO/EB and DAPI-stained HeLa cancer cells. After treatment of HeLa with 12.5 μM of **1**-**3**, apoptotic cells with apoptotic features, such as nuclear shrinkage and chromatin condensation, were found, as shown in Fig. 10. In this figure, yellow arrows show early apoptotic HeLa cells with membrane blebbing, which is seen at a fixed concentration of complexes **1**-**3**, and blue arrows exhibit late apoptotic cells with chromatin aggregation, that is highly condensed chromatin. Necrotic cells having uniform orange to red nuclei with a condensed structure are observed. The overall results indicate that complexes **1**-**3** induce cell death by necrosis, which is in good agreement with the above toxicity results.

4. Conclusions

In conclusion, we have synthesized an N,S donor Schiff base and its mononuclear Ni(II), Cu(II) and Zn(II) complexes. The characterization of these compounds was carried out using elemental analysis, FT-IR, UV-vis, ^{1}H NMR, ^{13}C NMR and mass spectrometry. Structural determination reveals that the complexes are discrete four coordinated, with a slightly distorted tetrahedral geometry. DFT calculations on all the complexes are in good agreement with the structural results obtained by X-ray crystallography. The CT-DNA/protein binding properties of the

complexes were examined by fluorescence spectra. All the fluorescence experiments show that the complexes **1**-**3** interact strongly with CT-DNA by an intercalative mode and BSA confirmed that the complexes have a greater binding affinity via the static mode. In this connection, the catecholase biomimetic catalytic activities of complexes **1**-**3** have been investigated. The results obtained show that all the complexes catalyze the aerobic oxidation of catechol to the corresponding o-quinone. Interestingly, all the three mononuclear complexes provide good phosphate-hydrolysis catalytic activity that is relevant to the binding of phosphate esters to the active site of an enzyme that catalyzes the phosphoryl transfer reaction. The cytotoxicity study shows that the complexes exhibit good cytotoxic activity against HeLa cell lines. Additionally, apoptotic tests indicate that the complexes show an apoptotic effect on HeLa cells. Based on the observed results, further studies are planned with these compounds against lung, bladder and breast cell lines.

Acknowledgement

The author N. N would like to thank P. Sugumar, Centre of Advanced Studies in Crystallography and Biophysics, University of Madras for his help in the valuable crystallographic discussions. We are sincerely thankful to the SAIF Punjab University, Chandigarh for the ESI mass facility and the Director, CAS in Botany, School of Life Sciences, University of Madras for providing laboratory facilities to perform the cell lines studies.

Electronic supplementary information (ESI) available

UV spectra of the compounds (Figs. S1-S4), FTIR spectra of the compounds (Figs. S5-S8), ^{1}H NMR spectra of the compounds (Figs. S9-S10), ^{13}C NMR spectra of compounds (Figs. S11-S13), ESI Mass spectrum of complex **1** (Fig. S14), kinetic Plot (3,5-DTBC) rate vs concentration of the complexes (Figs. S15-S17), kinetic plot (4-NPP) rate vs concentration of the complexes (Figs. S18-S20), DFT and experimental values of IR spectra (Table S1). The natural charge and electronic configuration (Table S2). CCDC reference numbers 1418965-1418968 for the compounds. For ESI data in CIF or other electronic format see DOI:

References

[1] D. Chatterjee, E. Ember, U. Pal, S. Ghosh, R.V. Eldik, Dalton Trans. 40 (2011) 10473-10480.

[2] C.X. Zhang, S.J. Lippard, Curr. Opin. Chem. Biol. 7 (2003) 481-489.

[3] X.Y. Wang, Anti-Cancer Agents Med. Chem. 10 (2010) 396-411.

[4] N.P. Farrell, Curr. Top. Med. Chem. 11 (2011) 2623-2631.

[5] J.J. Wilson, S.J. Lippard, Chem. Rev. 114 (2014) 4470-4495.

[6] X.Y. Wang, Z.J. Guo, Bioinorg. Med. Chem, ed. E. Alessio, Wiley- VCH Verlag GmbH & Co. KGaA, Weinheim. 97 (2011) 97-149.

[7] A.N. Montenegro, R. Carballo, J.M. Hermida-Ramón, E.M. Vázquez-López, Polyhedron 27 (2008) 2867-2876.

[8] R.K. Grasselli, Catal. Today 49 (1999) 141-153.

[9] R.J. Cross, P.D. Newman, R.D. Peacock, D. Stirling, J. Mol. Catal. 144 (1999) 273-284.

[10] M.R. Maurya, S. Dhaka,F. Avecilla, Polyhedron 81 (2014) 154-167.

[11] K.J. Ivin, J.C. Mol, Olefin Metathesis and Metathesis Polymerization, Academic Press, London, 1997.

[12] Q. He, C.H. Liang, S.J. Lippard, Proc. Natl. Acad. Sci. U. S. A. 97 (2000) 5768-5772.

[13] D.B. Zamble, Y. Mikata, C.H. Eng, K.E. Sandman, S.J. Lippard, J. Inorg. Biochem. 91 (2002) 451-462.

[14] V. Uma, M. Kanthimathi, T. Weyhermuller, B. U. Nair, J. Inorg. Biochem. 99 (2005) 2299-2307.

[15] C. Yan Gao, X. Qiao, Z.Y. Ma, Z.G. Wang, J. Lu, J.L. Tian, J.Y. Xub, S.P. Yan, Dalton Trans. 41 (2012) 12220-12232.

[16] P. Gentschev, N. Moller, B. Krebs, Inorg. Chim. Acta. 300 (2000) 442-452.

[17] M. Merkel, N. Mcller, M. Piacenza, S. Grimme, A. Rompel, B. Krebs, Chem. Eur. J. 11 (2005) 1201-1209.

[18] E. Monzani, L. Quinti, A. Perotti, L. Casella, M. Gullotti, L. Randaccio, S. Geremia, G. Nardin, P. Faleschini, G. Tabbi, Inorg. Chem. 37 (1998) 553-562.

[19] M. Gupta, P. Mathur, R.J. Butcher, Inorg. Chem. 40 (2001) 878-885.

[20] N.N. Murthy, M. Mahroof-Tahir, K.D. Karlin, Inorg. Chem. 40 (2001) 628-635.

[21] C.H. Kao, H.H. Wei, Y.H. Liu, G.H. Lee, Y. Wang, C.J. Lee, J. Inorg. Biochem. 84 (2001) 171-178.

[22] L. Que, W.B. Tolman, Nature 455 (2008) 333-340.

[23] E.B. Meunier, Biomimetic Oxidations Catalyzed by Transition Metal Complexes, Imperial College Press, London, 2000.

[24] A.J. Kirby, M. Younas, J. Chem. Soc. B. 1970, 510-513.

[25] E. L. Hegg, J.N. Burstyn, Coord. Chem. Rev. 173 (1998) 133-165.

[26] M. Komiyama, N. Takeda, H. Shigekawa, Chem. Commun. 1999, 1443-1452.

[27] R. Krämer, Coord. Chem. Rev.182 (1999) 243-261.

[28] H. Williams, B. Takasaki, J. Chin, Acc. Chem. Res. 32 (1999) 485-493.

[29] A. Blaskó, T.C. Bruice, Acc. Chem. Res. 32 (1999) 475-484.

[30] J.K. Bashkin, Curr. Opinion Chem. Biol. 3 (1999) 752-758.

[31] P. Molenveld, J.F.J. Engbersen, D.N. Reinhoudt, Chem. Soc. Rev. 29 (2000) 75.

[32] C. Hengge, Acc. Chem. Res. 35 (2002) 105-112.

[33] C. Lad, N.H. Williams, R. Wolfenden, Proc. Natl. Acad.Sci. U. S. A. 100 (2003) 5607-5610.

[34] A.G. Cassano, V.E. Anderson, M.E. Harris, J. Am.Chem. Soc. 124 (2002) 10964-10965.

[35] H. Linjalahti, G. Feng, J.C. Mareque-Rivas, S. Mikkola, N.H. Williams, J. Am. Chem. Soc. 130 (2008) 4232-4233.

[36] Y. Wang, W. Xiao, J.W. Mao, H. Zhou, Z.Q. Pan, J. Mol.Struct. 1036 (2013) 361-371.

[37] K. Yamaguchi, F. Akagi, S. Fujinami, M. Suzuki, M. Shionoya, S. Suzuki, Chem. Commun. (2001) 375-376.

[38] S.C. Batista, A. Neves, A.J. Bortoluzzi, I. Vencato, R.A. Peralta, B. Szpoganicz, V.V.E. Aires, H. Terenzi, P.C. Severino, Inorg. Chem. Commun. 6 (2003)1161-1165.

[39] S. Anbu, M. Kandaswamy, Inorg. Chim. Acta 385 (2012) 385 45-52.

[40] L. Zhu, O. dos Santos, C.W. Koo, M. Rybstein, L. Pape, J.W. Canary, Inorg. Chem. 42 (2003) 7912-7920.

[41] O. Iranzo, J.P. Richard, J.R. Morrow, Inorg. Chem. 43 (2004) 1743-1750.

[42] G. N. De Iuliis, G.A. Lawrance, S. Fieuw-Makaroff, Inorg. Chem. Commun. 3 (2000) 307-309.

[43] E.H. Serpersu, D. Shortle, A.S. Mildvan, Biochemistry 26 (1987) 1289-1300.

[44] S. Pollack, T. Uchida, D. Auld, J. Protein Chem. 2 (1983) 1-12.

[45] J.E. Thompson, F.D. Venegas, R.T. Raines, Biochemistry 33 (1994) 7408-7414.

[46] N. Nanjundan, P. Selvakumar, R. Narayanasamy, R.A. Haque, K. Velmurugan, R. Nandhakumar, T. Silambarasan and R. Dhandapani, J. Photochem. Photobiol. B 141 (2014) 176-185.

[47] M. Yazdanbakhsh, R. Takjoo, Struct. Chem. 19 (2008) 895-903.

[48] M.J. Frisch, G.W. Trucks, H.B. Schlegel, G.E. Scuseria, M.A. Robb, J.R. Cheeseman, G. Scalmani, V. Barone, B. Mennucci, G.A. Petersson, H. Nakatsuji, M. Caricato, X. Li, H.P. Hratchian, A.F. Izmaylov, J. Bloino, G. Zheng, J.L. Sonnenberg, M. Hada, M. Ehara, K. Toyota, R. Fukuda, J.Hasegawa, M. Ishida, T. Nakajima, Y. Honda, O. Kitao, H. Nakai, T. Vreven, J.A. Montgomery, J.E. Peralta, F. Ogliaro, M. Bearpark, J.J. Heyd, E. Brothers, K.N. Kudin, V.N. Staroverov, T. Keith, R. Kobayashi, J. Normand, K. Raghavachari, A. Rendell, J.C. Burant, S.S. Iyengar, J. Tomasi, M. Cossi, N. Rega, J.M. Millam, M. Klene, J.E. Knox, J.B. Cross, V. Bakken, C. Adamo, J. Jaramillo, R. Gomperts, R.E. Stratmann, O. Yazyev, A.J. Austin, R. Cammi, C. Pomelli, J.W. Ochterski, R.L. Martin, K. Morokuma, V.G. Zakrzewski, G.A. Voth, P. Salvador, J.J. Dannenberg, S. Dapprich, A.D. Daniels, O. Farkas, J.B. Foresman, J.V. Ortiz, J. Cioslowski, D.J. Fox, Gaussian 09, Inc. Wallingford. CT (2010).

[49] P. Vijayan, P. Viswanathamurthi, P. Sugumar, M.N. Ponnuswamy, M.D. Balakumaran, P. T. Kalaichelvan, K. Velmurugan, R. Nandhakumar, R.J. Butcher, Inorg. Chem. Front. 2 (2015) 620-639.

[50] F.N.F. How, K.A. Crouse, M.I.M. Tahir, D.J. Watkin, J. Chem. Crystallogr. 39 (2009) 894-897.

[51] P. Vijayan, P. Viswanathamurthi, V. Silambarasan, D. Velmurugan, K. Velmurugan, R. Nandhakumar, R.J. Butcher, T. Silambarasan, R. Dhandapani, J. Organomet. Chem. 768 (2014) 163-177.

[52] V. Krishnakumar, R. John Xavier, Indian J. Pure Appl. Phys. 41 (2003) 597-601.

[53] G.F. de Sousa, D.X. West, C.A. Brown, J.K. Swearingen, J. Valdés-Martínez, R.A. Toscano, S. Hernández-Ortega, M. Hörner, A.J. Bortuluzzi, Polyhedron 19 (2000) 841-847.

[54] E. Bermejo, A. Carballo, A. Castíñeiras, R.R. Domíniguez, C. Maichle- Mössmer, J. Strähle, D.X. West, Polyhedron 18 (1999) 3695-3702.

[55] X. West, M.A. Lockwood, A.E. Liberta, X. Chen, R.D. Willet, Transition Met. Chem. 18 (1993) 221-227.

[56] H. Ullah, A. Rauf, Z. Ullah, F. Sattar, M. Anwar, A.A. Shah, G. Uddin, K. Ayub, Spectrochim. Acta. Mol. Biomol. Spectros. 118 (2014) 210-214.

[57] D. Kalita, R.C. Deka, N.S. Islam, Inorg. Chem. Commun.10 (2007) 45-48.

[58] Q. Yu, Y. Liu, J. Zhang, F. Yang, D. Sun, D. Liu, Y. Zhou, J. Liu, Metallomics 5 (2013) 222-231.

[59] K. Bielawaski, S. Wolczynski, A. Bielawska, Biol. Pharm. Bull. 24 (2001) 704-706.

[60] L.A. Lipscomb, F.X. Zhou, S.R. Presnell, R.J. Woo, M.E. Peek, R.R. Plaskon, L.D. Williams, Biochemistry 35 (1996) 2818-2823.

[61] F. Arjmand, F. Sayeed, M. Muddassir, J. Photochem.Photobiol. B. 103 (2011) 166-179.

[62] J. R. Lakowicz, G. Weber, Biochemistry 12 (1973) 4161-4170.

[63] G. Psomas, J. Inorg. Biochem. 102 (2008) 1798-1811.

[64] K.D. Karlin, B.I. Cohen, J.C. Hayes, A. Farooq, J. Zubieta, Inorg. Chem. 26 (1987) 147-153.

[65] J.R. Lakowicz, G. Weber, Biochemistry 12 (1973) 4161-4170.

[66] H. Gao, L.D. Lei, J.Q. Liu, Q. Kong, X.G. Chen, Z.D. Hu, J. Photochem. Photobiol. A 167 (2004) 213-221.

[67] P.B. Kandagal, S.M.T. Shaikh, D.H. Manjunatha, J. Seetharamappa, B.S. Nagaralli, J. Photochem. Photobiol. A 189 (2007) 121-127.

[68] V. Anbazhagan, R. Renganathan, J. Lumin. 128 (2008) 1454-1458.

[69] P. Banerjee, S. Ghosh, A. Sarkar, S.C. Bhattacharya, J. Lumin. 131 (2011) 316-321.

[70] T. Chattopadhyay, M. Mukherjee, A. Mondal, P. Maiti, A. Banerjee, K.S. Banu, S. Bhattacharya, B. Roy, D.J. Chattopadhyay, T.K. Mondal, M. Nethaji, E Zangrando, D. Das, Inorg. Chem. 49 (2010) 3121-3129.

[71] D. Gstteschi, A. Scozzafava, Inorg. Chim. Acta. 21 (1977) 223-227.

[72] Mendoza-Quijano, M.R. Ferrer-Sueta, G. Flores-Álamo, M. Aliaga-Alcalde, N. Gómez-Vidales, V. Ugalde-Saldívara, V.M. Gasque, L. Dalton Trans. 41 (2012) 4985-4997.

[73] Ackermann, J.Meyer, F. Kaifer, E. Pritzkow, H. Chem. Eur. J. 8 (2002) 247-258.

[74] Kodera, M. Kawata, T. Kano, K. Tachi, Y. Itoh, S; Kojo, S. Bull. Chem. Soc. Jpn. 76 (2003) 1957-1964.

[75] Koval, I.A. Selmeczi, K. Belle, C. Philouze, C. Saint-Aman, E. Gautier- Luneau, I. Schuitema, A.M. Vliet, M.V. Gamez, P. Roubeau, O. Luken, M. Krebs, B. Lutz, M. Spek, A.L. Pierre, J.L. Reedijk, J. Chem. Eur. J. 12 (2006) 6138-6150.

[76] J. Kaizer, T. Csay, G. Speier, M. Giorgi, J. Mol. Catal. A: Chem. 329 (2010) 71-76.

[77] N.A. Rey, A. Neves, A. Bortoluzzi, C.T. Pich, H. Terenzi, Inorg. Chem. 46 (2007) 348-350.

[78] N.I.Jakab, A.Jancso, T.Gajda, B. Gyurcsik, A. Rockenbauer, J. Inorg. Biochem. 102 (2008) 1438-1448.

[79] S. Sreedaran, K. Shanmuga Bharathi, A. Kalilur Rahiman, L. Jagadish, V. Kaviyarasan, V. Narayanan, J. Incl. Phenom. Macrocycl. Chem. 66 (2010) 297-306.

[80] S. Kasibhatla, B. Tseng, Mol. Cancer Ther. 2 (2003) 573-580.

[81] L. Strekowski, B. Wilson, Mutat. Res. 623 (2007) 3-13.

[82] W. A. Denny, Curr. Med. Chem. 9 (2002) 1655-1665.

[83] H.K. Liu, J.P. Sadler, Acc. Chem. Res. 44 (2011) 349-359.

[84] R. Martinez, L.C. Garcia, Curr. Med. Chem. 12 (2005) 127-151.

Fig. 1. ORTEP view of **[H-(Ap-sadtc)]** and its complexes **1**-**3**. Thermal ellipsoids are drawn at the 25% probability level.

Fig. 2. Surface plots of the frontier orbitals along with their energies of **[H-(Ap-sadtc)]** and its complexes **1**-**3**, using the B3LYP/6-311G functional.

Fig. 3. Emission spectra and Scatchard plots of complexes **1**-**3** (25 μM) in the presence of increasing concentrations of CT DNA

Fig. 4. Fluorescence spectra and Stern–Volmer plots of the complexes **1**-**3** (0-50 μM) with EB bound CT-DNA. Arrows show the decreasing emission intensity with increasing concentrations of the complexes.

Fig. 5. Emissive spectra and Stern–Volmer plots of BSA upon titration with complexes **1**-**3**. The arrow shows the change upon increasing the complex concentration.

Fig. 6. Scatchard plots of Log[Fo-F/F] *vs* Log[Q] for complexes **1**-**3**.

Fig. 7. Time resolved emission spectra of the reaction and Lineweaver–Burk plot for complexes **1**-**3** with 3,5-DTBC after addition of the complexes with 15 min. time intervals.

Fig. 8. Phosphate hydrolysis emission spectra and Lineweaver–Burk plots for complexes **1**-**3**.

Fig. 9. Effect of complexes **1**-**3** on normal vero and HeLa cancer cell viability (%) at different concentrations.

Fig. 10. AO/EB (1A, 2A, 3A) and DAPI (1B, 2B, 3B) stained HeLa cells at 24 h incubation after treatment with complexes **1**-**3**. The yellow, blue and red arrows show early apoptotic cells with blebbing, late apoptosis and necrotic cells respectively.

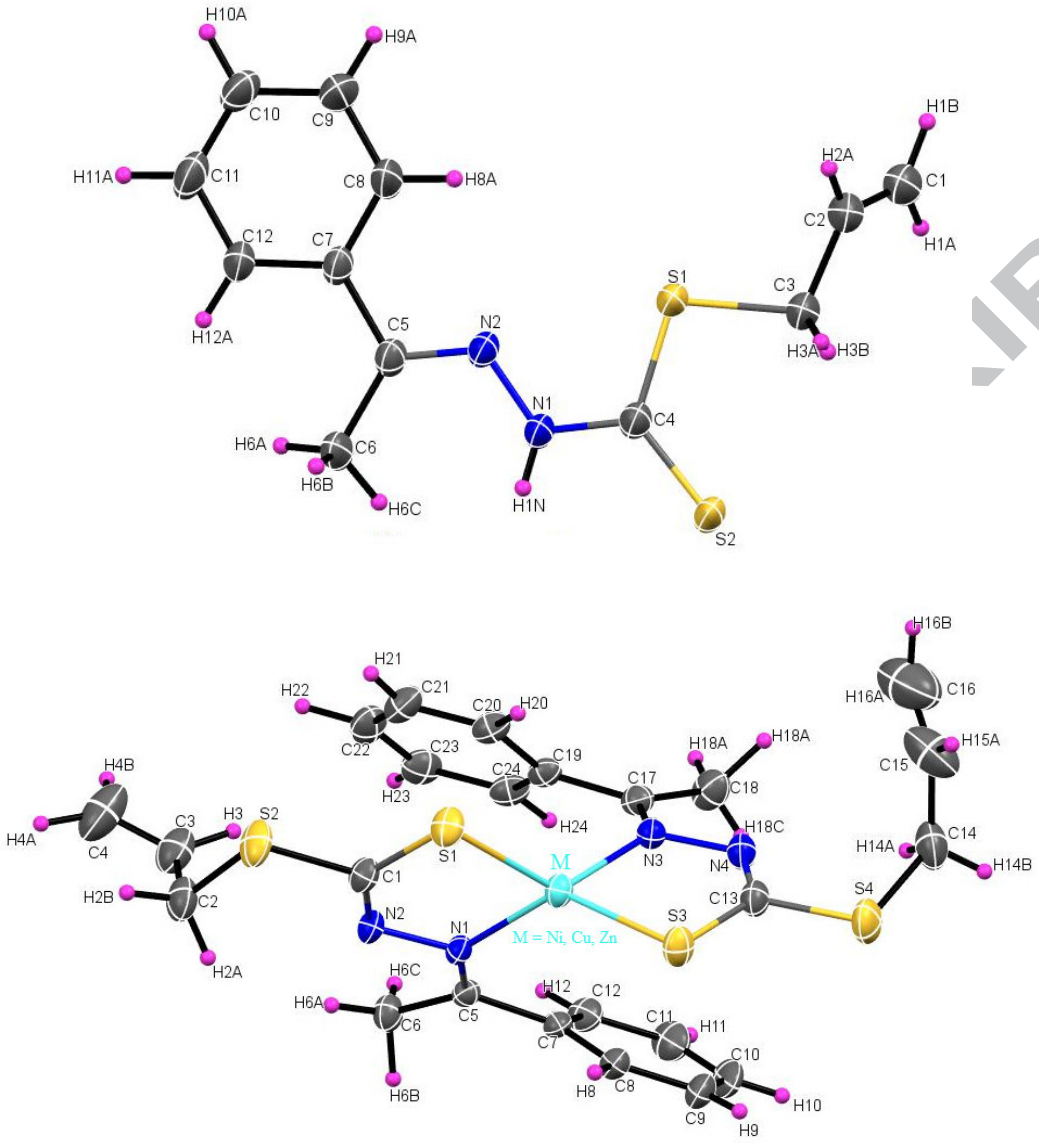

Fig. 1. ORTEP view of **[H-(Ap-sadtc)]** and its complexes **1-3**. Thermal ellipsoids are drawn at the 25% probability level.

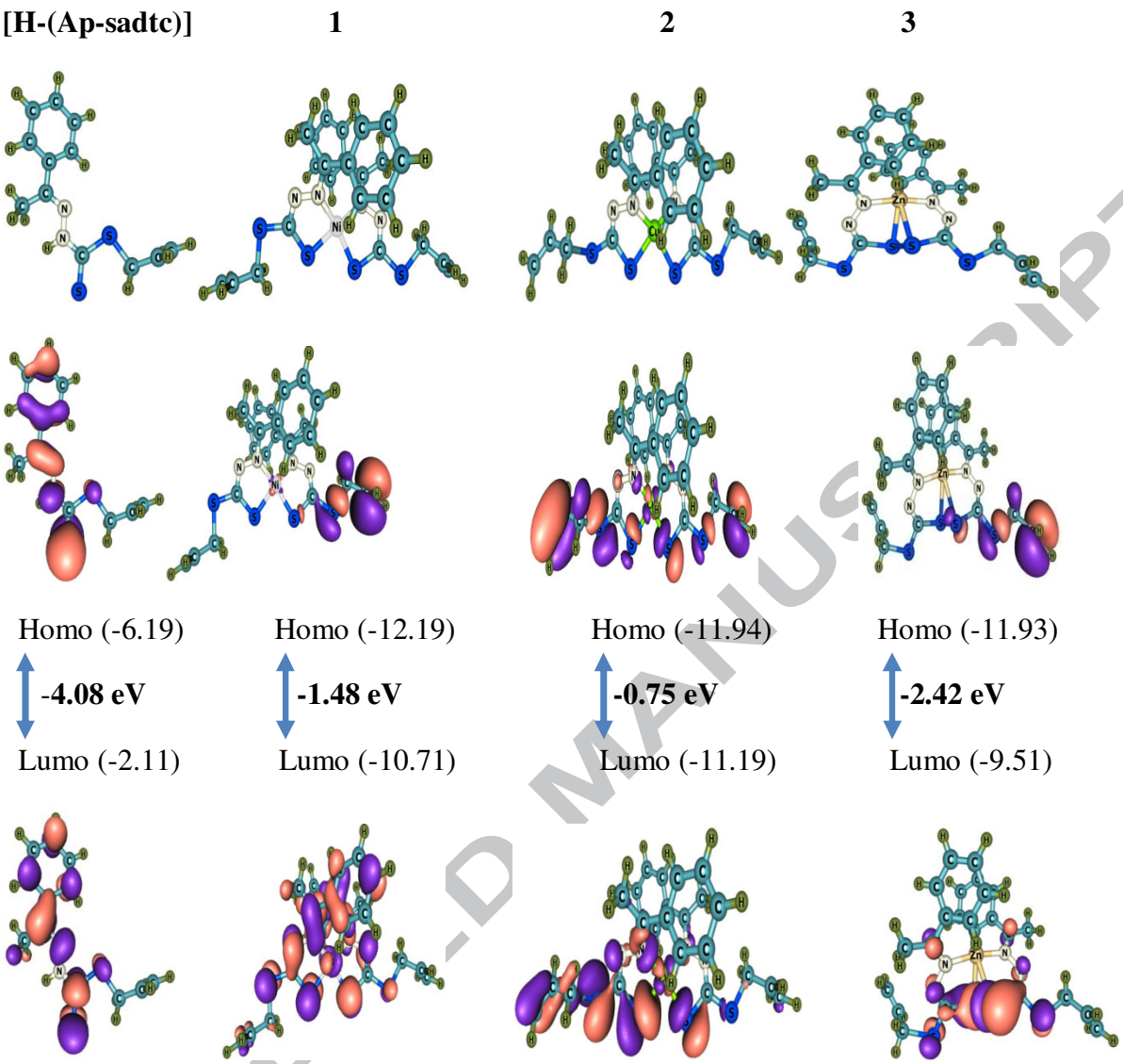

Fig. 2. Surface plots of the frontier orbitals along with their energies of **[H-(Ap-sadtc)]** and its complexes **1**-**3**, using the B3LYP/6-311G functional.

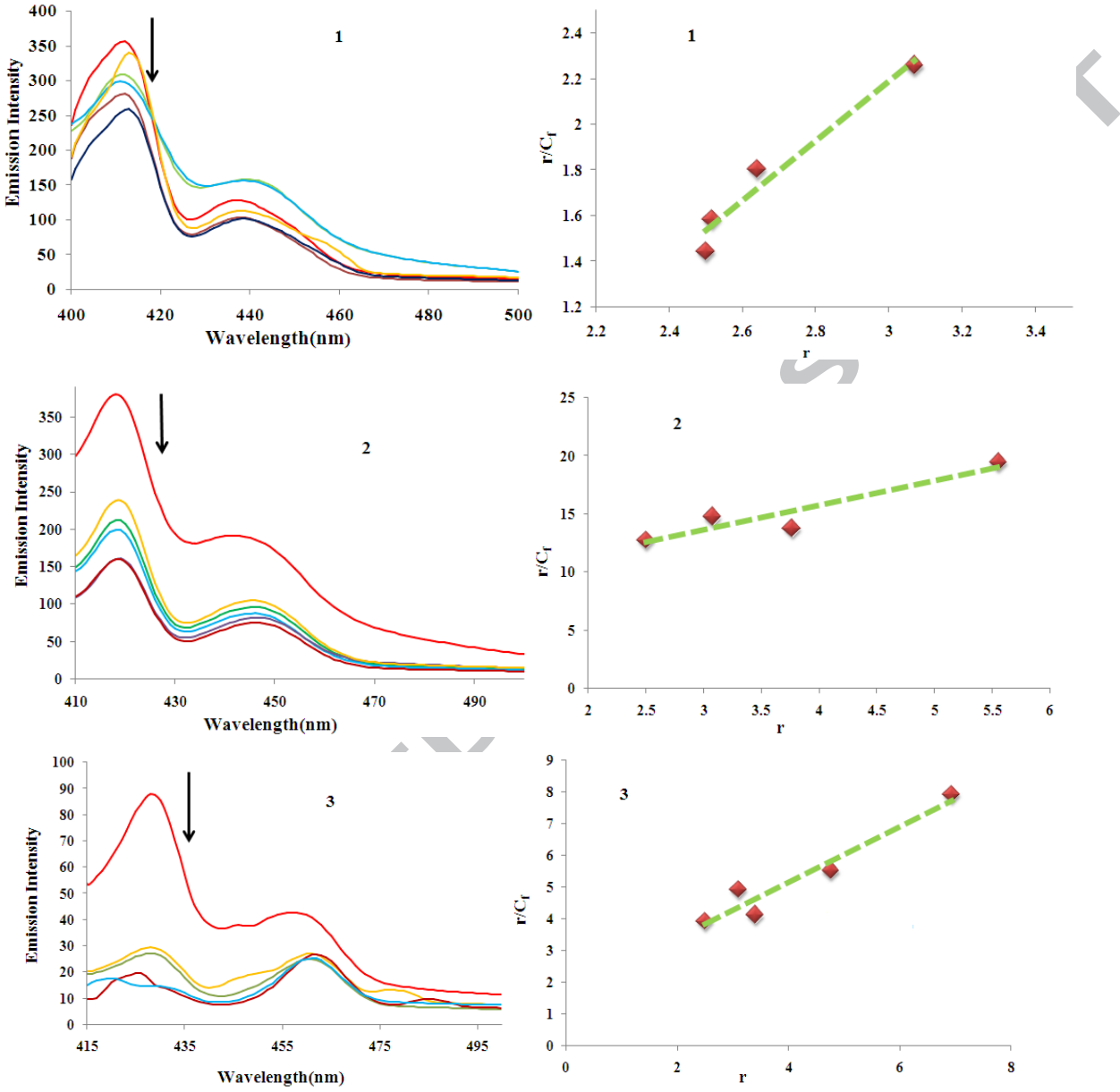

Fig. 3. Emission spectra and Scatchard plots of complexes **1-3** (25 μM) in the presence of increasing concentrations of CT-DNA

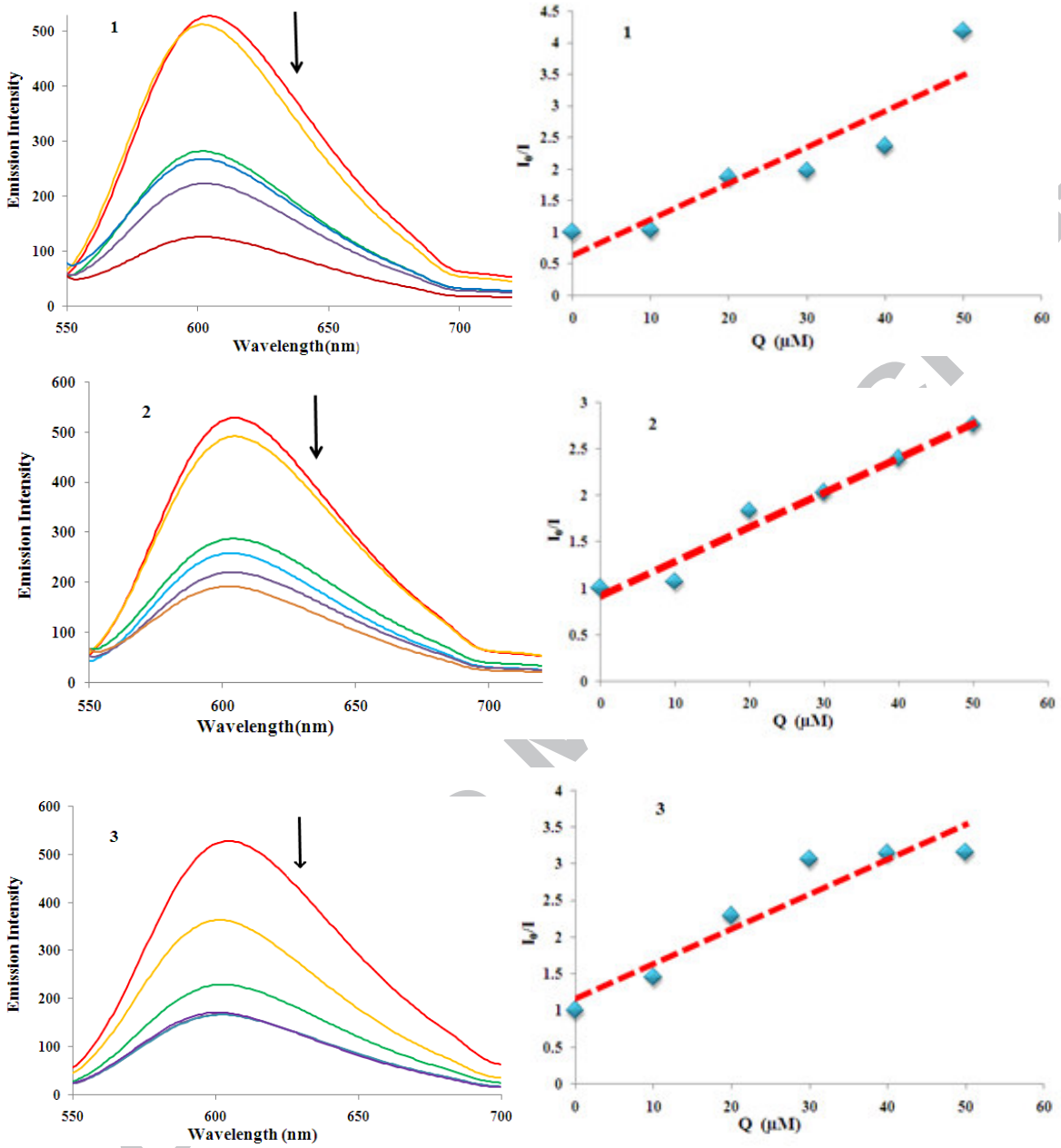

Fig. 4. Fluorescence spectra and Stern–Volmer plots of the complexes **1**-**3** (0–50 μM) with EB bound CT-DNA. Arrows show the decreasing emission intensity with increasing concentrations of the complexes.

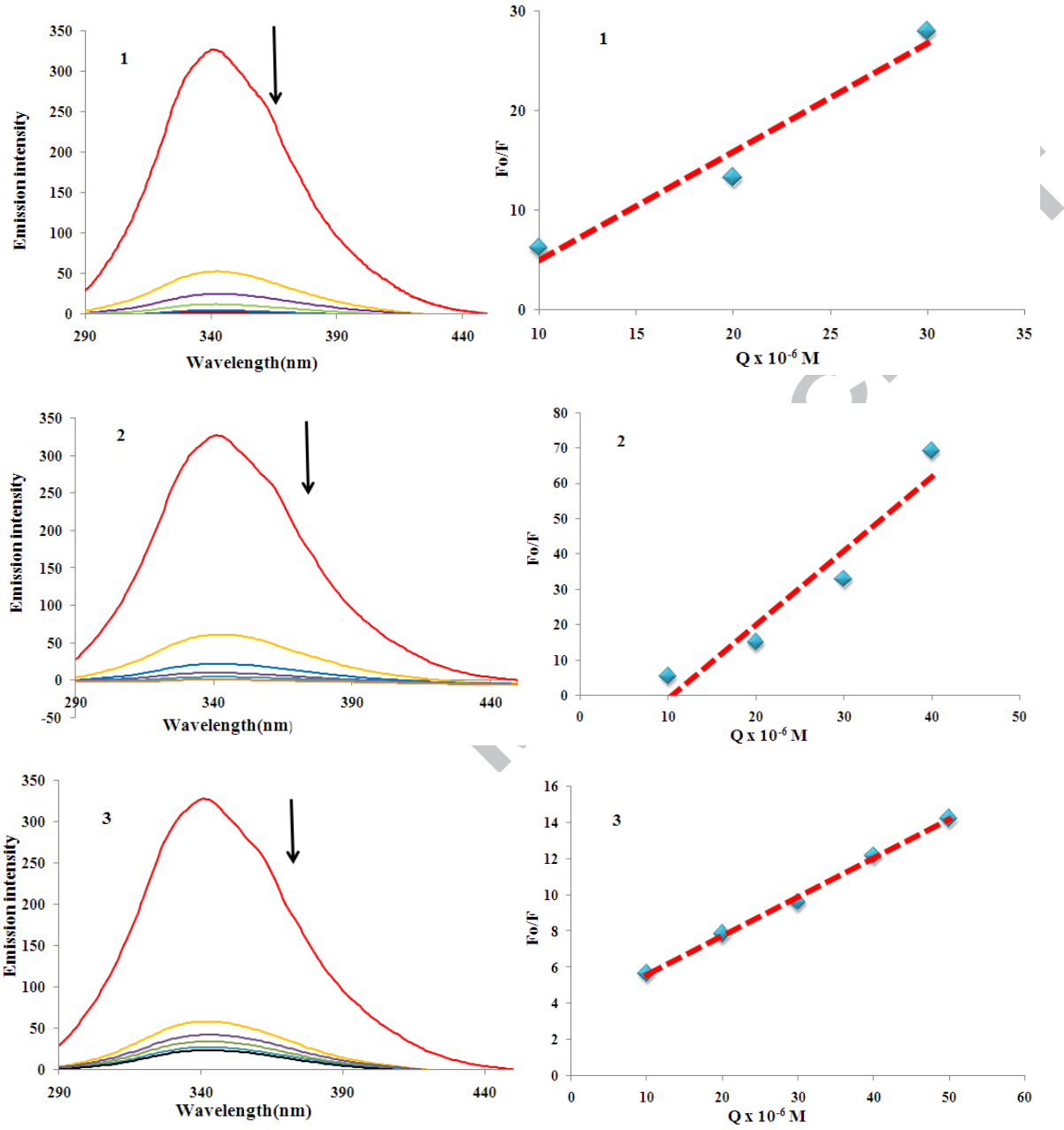

Fig. 5. Emissive spectra and Stern–Volmer plots of BSA upon titration with complexes **1**-**3**. The arrow shows the change upon increasing the complex concentration.

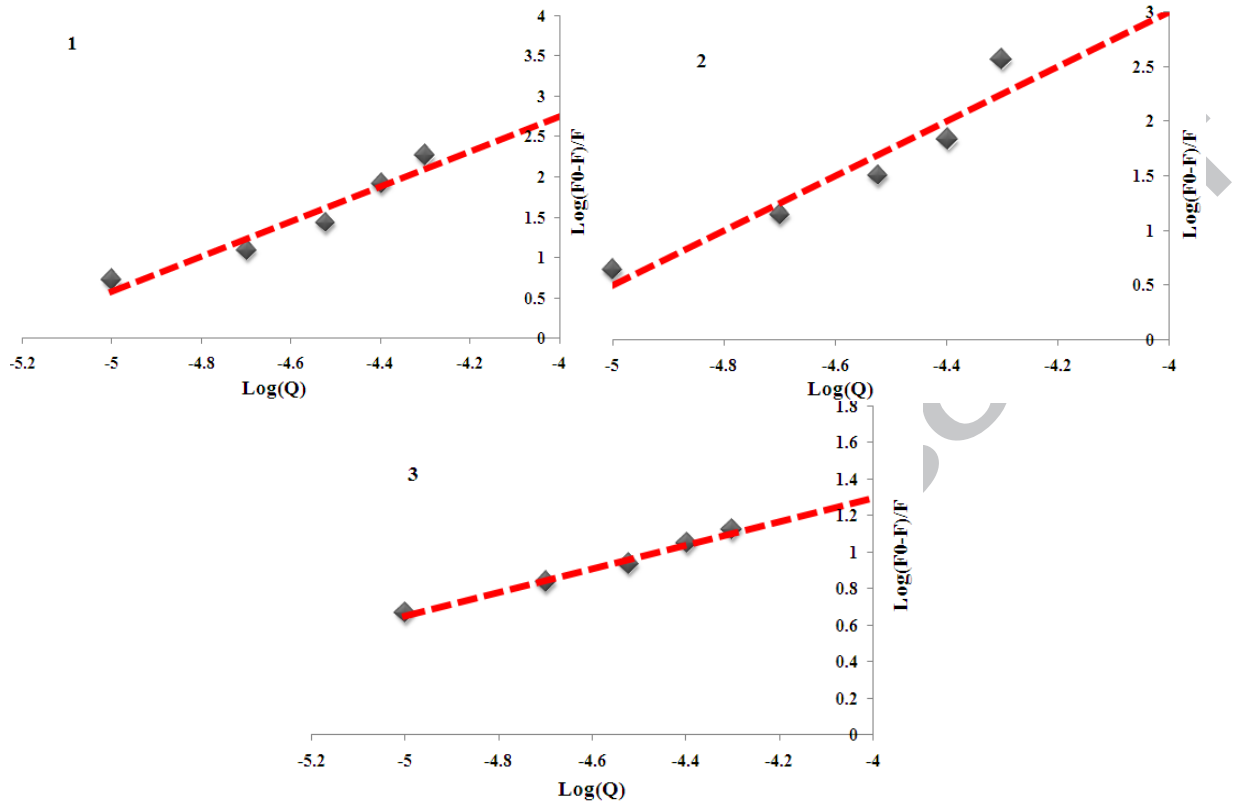

Fig. 6. Scatchard plots of Log[Fo-F/F] *vs* Log[Q] for complexes **1**-**3**.

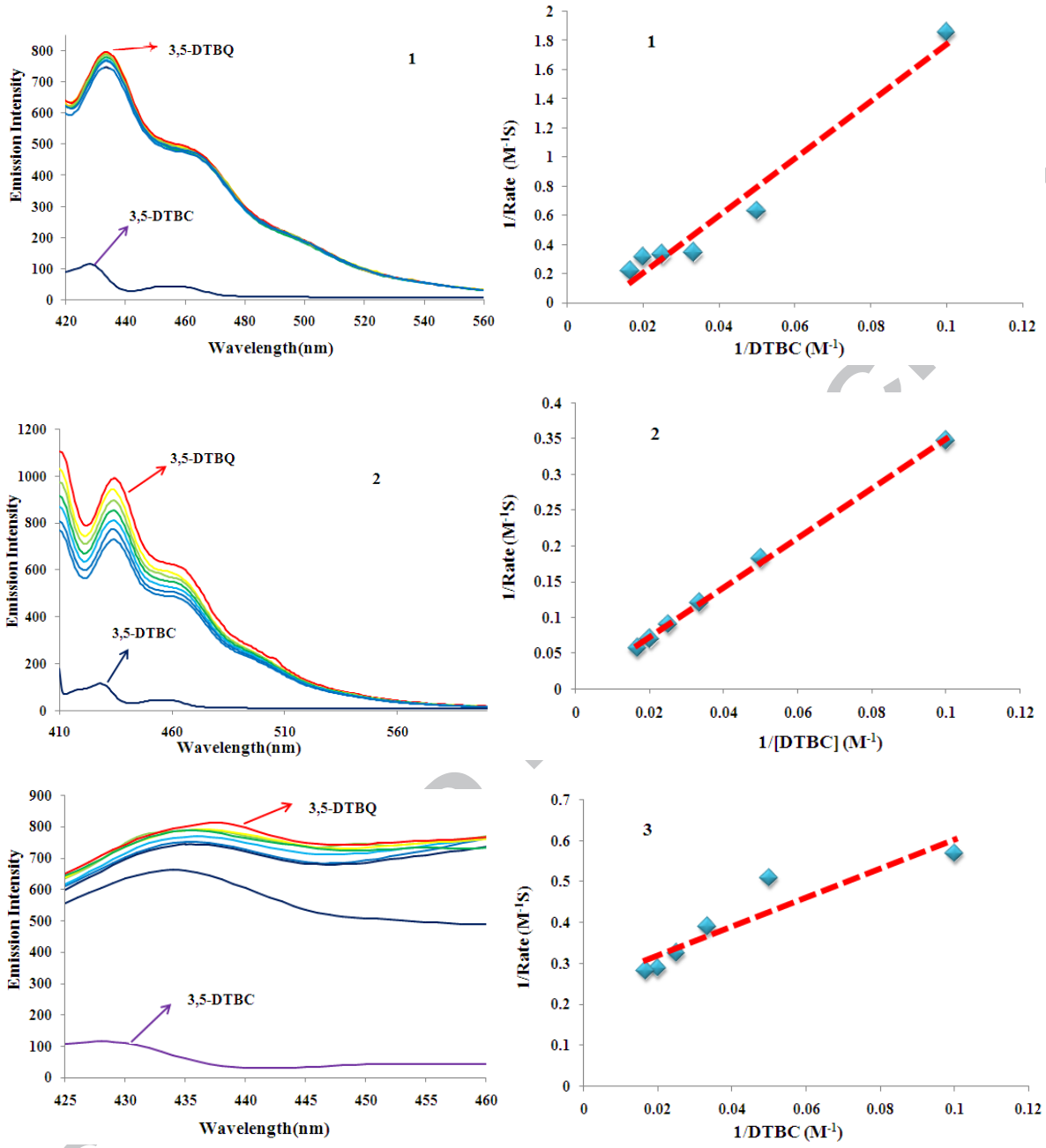

Fig. 7. Time resolved emission spectra of the reaction and Lineweaver–Burk plot for complexes **1-3** with 3,5-DTBC after addition of the complexes with 15 min. time intervals.

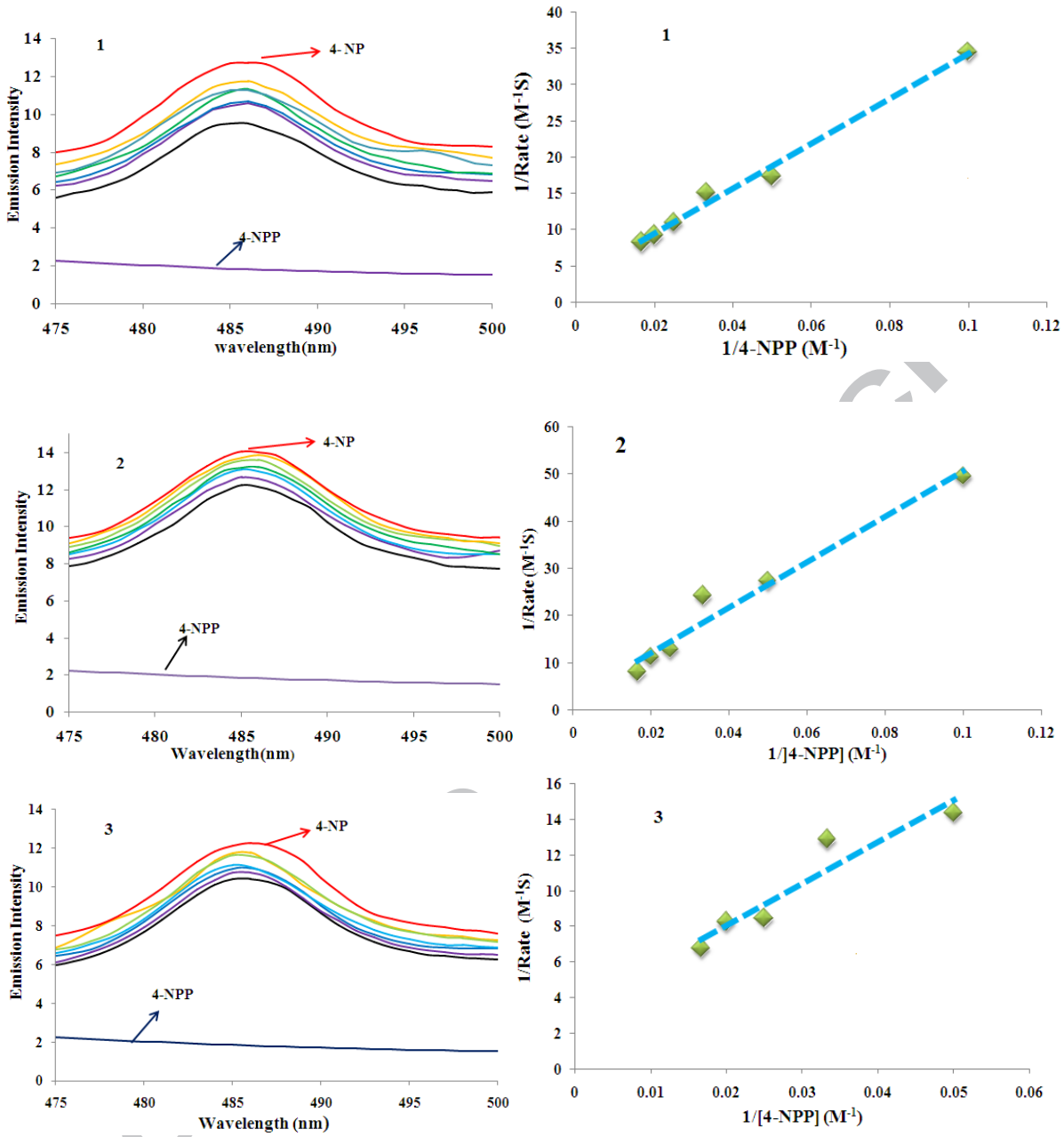

Fig. 8. Phosphate hydrolysis emission spectra and Lineweaver–Burk plots for complexes **1-3.**

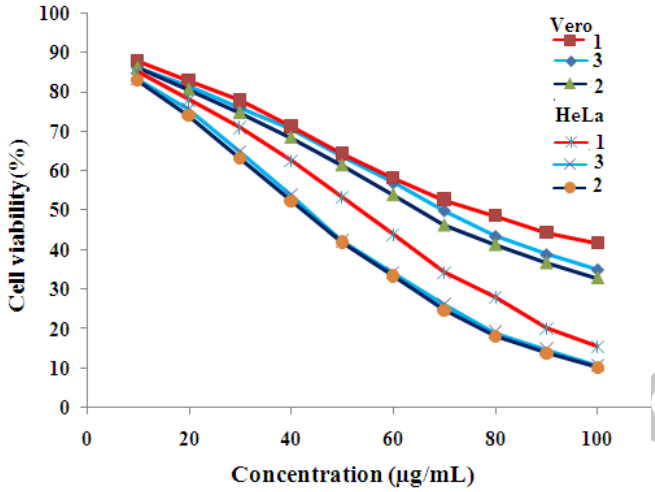

Fig. 9. Effect of complexes **1**-**3** on normal vero and HeLa cancer cell viability (%) at different concentrations.

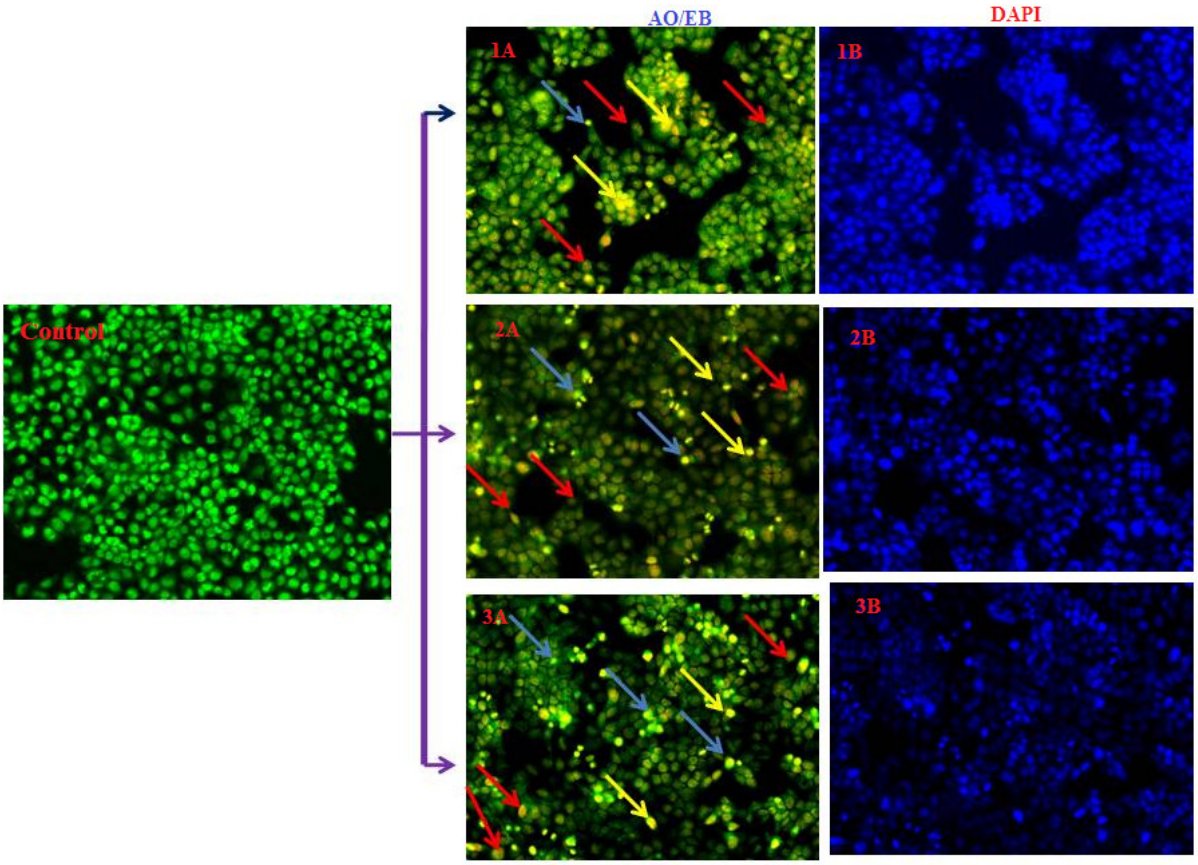

Fig. 10. AO/EB (1A, 2A, 3A) and DAPI (1B, 2B, 3B) stained HeLa cells at 24 h incubation after treatment with complexes **1**-**3**. The yellow, blue and red arrows show early apoptotic cells with blebbing, late apoptosis and necrotic cells respectively.

Table 1 Crystal data collection of **[H-(Ap-sadtc)]** and complexes **1**-**3**.

Table 2 Experimental, DFT data for selected bonds lengths (Å) and angles (^{o}) of **[H-(Ap-sadtc)]** and its complexes **1**-**3**.

Table 3 Electronic properties of **[H-(Ap-sadtc)]** and its complexes **1**–**3** at the B3LYP/6-311G level.

Table 4 CT-DNA binding constant (K_b), quenching constant (K_{sv}) and apparent binding constant (K_{app}) values for complexes **1**-**3**.

Table 5 Quenching constant (K_q), binding constant (K_{bin}) and number of binding sites (n) for the interactions of the complexes with BSA.

Table 6 Kinetic parameters for complexes **1**-**3** in DMSO solution.

Table 7 Phosphate hydrolysis parameters for complexes **1**-**3**.

Table 8 *In vitro* cytotoxicity of the complexes **1-3** in Vero and HeLa cell lines.

Table 1

Crystal data collection of **[H-(Ap-sadtc)]** and its complexes **1**-**3**.

	[H-(Ap-sadtc)]	**1**	**2**	**3**
Chemical formula	$C_{12}H_{14}N_2S_2$	$C_{24}H_{26}N_4NiS_4$	$C_{24}H_{26}CuN_4S_4$	$C_{24}H_{26}N_4S_4Zn$
Formula weight (g/mol)	250.37	557.44	562.27	564.10
Temperature (K)	220(2)	220(2)	230(2)	230(2)
Wavelength (Å)	1.54178	1.54178	1.54178	1.54178
Crystal system	Triclinic	Monoclinic	Orthorhombic	Monoclinic
Space group	P *-1*	P *21/n*	P *21 21 2*	P *21/n*
a (Å)	12.2111(5)	9.0667(2)	8.9903(5)	8.9523(4)
b (Å)	13.8806(7)	21.5224(5)	17.7705(10)	23.3868(9)
c (Å)	13.9619(7)	13.4599(3)	8.4076(4)	12.8090(5)
α (°)	14.479(3)	90	90	90
β (°)	113.094(3)	92.9730(9)	90	99.505(2)
γ (°)	91.864(3)	90	90	90
Volume $Å^3$	1926.66(17)	2622.99(10)	1343.22(12)	2644.95(19)
Z	6	4	2	4
Density (cal) (g/cm^3)	1.295	1.412	1.39	1.417
Absorption coefficient (mm^{-1})	3.542	4.195	4.201	4.391
F(000)	792	1160	582	1168
Theta range for data collection	3.60 to 68.28°	3.88 to 59.04°	4.98 to 68.21°	3.78 to 70.23°
Index ranges	-14<=h<=12, -16<=k<=16, -16<=l<=16	-14<=h<=12, -16<=k<=16, -16<=k<=16,	-10<=h<=10, -18<=k<=21 -10<=l<=10,	-10<=h<=10, -28<=k<=28, -15<=l<=13
Reflections collected	22324	15868	22322	27268
Independent reflections	6889 [R(int) = 0.0662]	3748 [R(int) = 0.0217]	2440 [R(int) = 0.0292]	4930 [R(int) = 0.0398]
Absorption correction	multi-scan	multi-scan	multi-scan	multi-scan
Max. and min. transmission	0.9330 and 0.6370	0.7300 and 0.5360	0.6330 and 0.5530	-
Refinement method	Full-matrix least-squares	Full-matrix least-squares	Full-matrix least-squares	Full-matrix least-squares

	on F^2	on F^2	on F^2	on F^2
Function minimized	$\Sigma\, w(F_o^2 - F_c^2)^2$	$\Sigma\, w(F_o^2 - F_c^2)^2$	$\Sigma\, w(F_o^2 - F_c^2)^2$	$\Sigma\, w(F_o^2 - F_c^2)^2$
Goodness-of-fit on F^2	1.174	1.134	0.993	1.159
Data / restraints / parameters	6889 / 3 / 448	3748 / 0 / 403	2440 / 0 / 203	4930 / 0 / 390
Δ/σ_{max}	0.004	0.006	0.233	0.007
Final R indices data; $I>2\sigma(I)$	4411, R1 = 0.0574, wR2 = 0.1390	3577, R1 = 0.0239, wR2 = 0.0844	2407, R1 = 0.0232, wR2 = 0.0725	4454, R1 = 0.0312, wR2 = 0.0969
R indices (all data)	R1 = 0.0988, wR2 = 0.1576	R1 = 0.0249, wR2 = 0.0856	R1 = 0.0235, wR2 = 0.0729	R1 = 0.0346, wR2 = 0.1002

Table 2

Experimental, DFT data for selected bonds lengths (Å) and angles (°) of **[H-(Ap-sadtc)]** and its complexes **1**-**3**.

Compound	Bond length (Å)	Experimental	DFT	Bond Angle (°)	Experimental	DFT
[H-(Ap-sadtc)]	S1-C4	1.743(4)	1.744	C4-N1-N2	117.8(3)	121.92
	S2-C4	1.667(3)	1.706	N2-N1-H1N	129.(3)	122.02
	S1-C3	1.822(4)	1.825	N1-C4-S2	121.6(3)	113.39
	N1-N2	1.376(4)	1.379	C7-C8-C9	121.2(4)	120.69
	N1-C4	1.343(5)	1.362	C8-C7-C12	117.2(3)	118.34
	N2-C5	1.294(5)	1.305	S2-C4-S1	125.1(2)	126.33
	C5-C6	1.496(5)	1.512	N1-C4-S1	113.3(3)	122.72
	C2-C3	1.491(6)	1.493			
	C1-C2	1.282(6)	1.335			
1	Ni1-N1	1.9320(13)	1.929	N3-Ni1-N1	100.91(5)	106.52
	Ni1-N3	1.9254(12)	1.93	N3-Ni1-S1	165.17(4)	158.8
	Ni1-S1	2.1548(5)	2.239	N1-Ni1-S1	86.32(4)	159.66
	Ni1-S3	2.1583(5)	2.209	C9-S1-Ni1	93.95(6)	94.81
	N2-C9	1.282(2)	1.491	C21-S3-Ni1	93.59(5)	94.83
	N3-C19	1.296(2)	1.335	N3-Ni1-S3	85.40(4)	86.13
	N2-C9	1.282(2)	1.319	S1-Ni1-S3	90.970(18)	86.91
	N1-N2	1.4186(19)	1.363			
	N3-N4	1.4185(18)	1.39			
	S2-C9	1.7524(16)	1.804			
	S3-C21	1.7420(17)	1.777			
2	Cu1-N1	2.0011(18)	2.014	N3-Cu1-N1	101.62(11)	111.75
	Cu1-N1	2.0011(18)	1.971	N3-Cu1-S1	151.13(6)	154.18
	Cu1-S1	2.2362(7)	2.335	N1-Cu1-S1	85.40(6)	85.41
	Cu1-S1	2.2363(7)	2.316	N3-Cu1-S3	85.40(6)	85.47
	C1-N2	1.287(3)	1.317	S3-Cu1-S1	101.98(4)	107.99

	C1-S2	1.758(2)	1.81	C1-S1-Cu1	92.12(8)	92.46
	N1-N2	1.396(3)	1.419	N2-N1-Cu1	116.80(13)	118.16
	S1-C1	1.739(2)	1.778			
	S2-C2	1.805(4)	1.804			
3	Zn1-N1	2.0546(15)	1.973	N1-Zn1-N3	108.48(6)	100.75
	Zn1-N1	2.0546(15)	1.972	S3-Zn1-S1	115.13(2)	91.88
	Zn1-S1	2.2817(5)	2.27	N1-Zn1-S1	87.38(4)	85.7
	Zn1-S3	2.28145)	2.272	N1-Zn1-S1	87.38(4)	85.63
	N3-N4	1.402(2)	1.402	N3-Zn1-S1	130.89(4)	164.11
	S1-C1	1.741(2)	1.789	N1-Zn1-S3	133.31(4)	164.45
	S3-C13	1.737(2)	1.779	C1-S1-Zn1	91.89(6)	91.21
				C13-S3-Zn1	91.75(7)	91.06
				N2-N1-Zn1	115.53(11)	117
				N4-N3-Zn1	114.86(11)	117.14

Table 3

Electronic properties of **[H-(Ap-sadtc)]** and its complexes **1**–**3** at the B3LYP/6-311G level.

QM descriptors	**[H-(Ap-sadtc)]**	**1**	**2**	**3**
Single point energy	-1371.52	-4381.74	-4249.56	-4520.62
Hardness	-4.08	-1.48	-0.75	-2.42
Chemical potential	-4.15	-11.45	-11.56	-10.72
Electrophilicity	2.0198	44.09	89.08	23.74

Table 4

CT-DNA binding constant (K_b), quenching constant (K_{sv}) and apparent binding constant (K_{app}) values for complexes **1**-**3.**

Complex	K_b (M^{-1})	K_{sv} (M^{-1})	K_{app} (M^{-1})
1	1.30×10^{6}	5.7×10^{4}	1.31×10^{5}
2	2.09×10^{6}	3.7×10^{4}	2.02×10^{5}
3	8.8×10^{5}	4.7×10^{4}	1.59×10^{5}

Table 5

Quenching constant (K_q), binding constant (K_{bin}) and number of binding sites (n) for the interactions of complexes with BSA.

Complex	K_{SV}	K_q (M^{-1})	K_{bin} (M^{-1})	'n'
1	$4.0x10^6$	$4.0x10^{14}$	$7.16x10^6$	1.2
2	$8.0x10^6$	$8.0x10^{14}$	$4.3x10^9$	1.8
3	$2.14x10^4$	$2.14x10^{12}$	$7.6\ x10^3$	0.64

Table 6

Kinetic parameters for complexes **1**-**3** in DMSO solution.

Complex	K_m(M)	V_{max}(MS^{-1})	K_{cat} (h^{-1})
1	253×10^{-4}	22.72×10^{-4}	253
2	864×10^{-4}	250×10^{-4}	864
3	106×10^{-4}	5.460×10^{-4}	106

Table 7

Phosphate hydrolysis parameters for complexes **1**-**3**.

Complex	K_m(M)	V_{max}(MS^{-1})	K_{cat} (h^{-1})
1	95.26×10^{-3}	0.303×10^{-3}	1905
2	191.5×10^{-3}	0.39×10^{-3}	3831
3	70.11×10^{-3}	0.299×10^{-3}	1402

Table 8

In vitro cytotoxicity of the complexes **1-3** in Vero and HeLa cell lines.

Compound	IC_{50}(μM)	
	Vero	HeLa
1	68.51±3.44	39.74±1.79
2	63.86±2.26	38.34±2.23
3	77.75±1.77	48.32±1.02
Cisplatin	-	35.7±0.0950

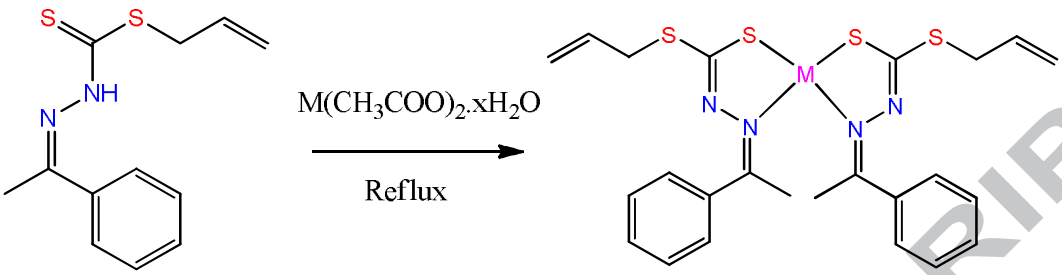

M= Ni, Cu, Zn

Scheme 1 Synthetic route for complexes **1**-**3**.

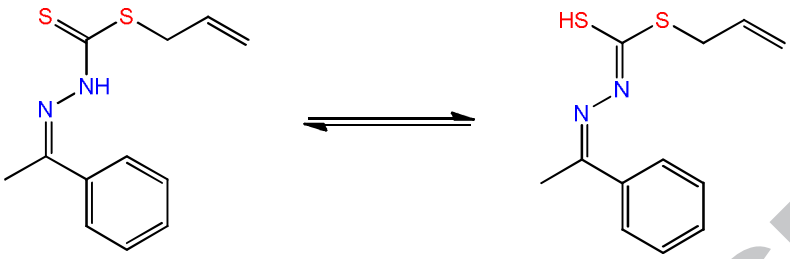

Thione Thiol

Scheme 2 Tautomeric forms of **[H-(Ap-sadtc)].**

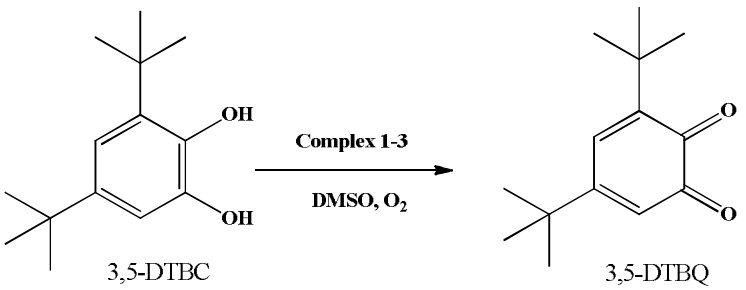

Scheme 3 Oxidation process of 3,5-DTBC to 3,5-DTBQ by complexes **1-3**.

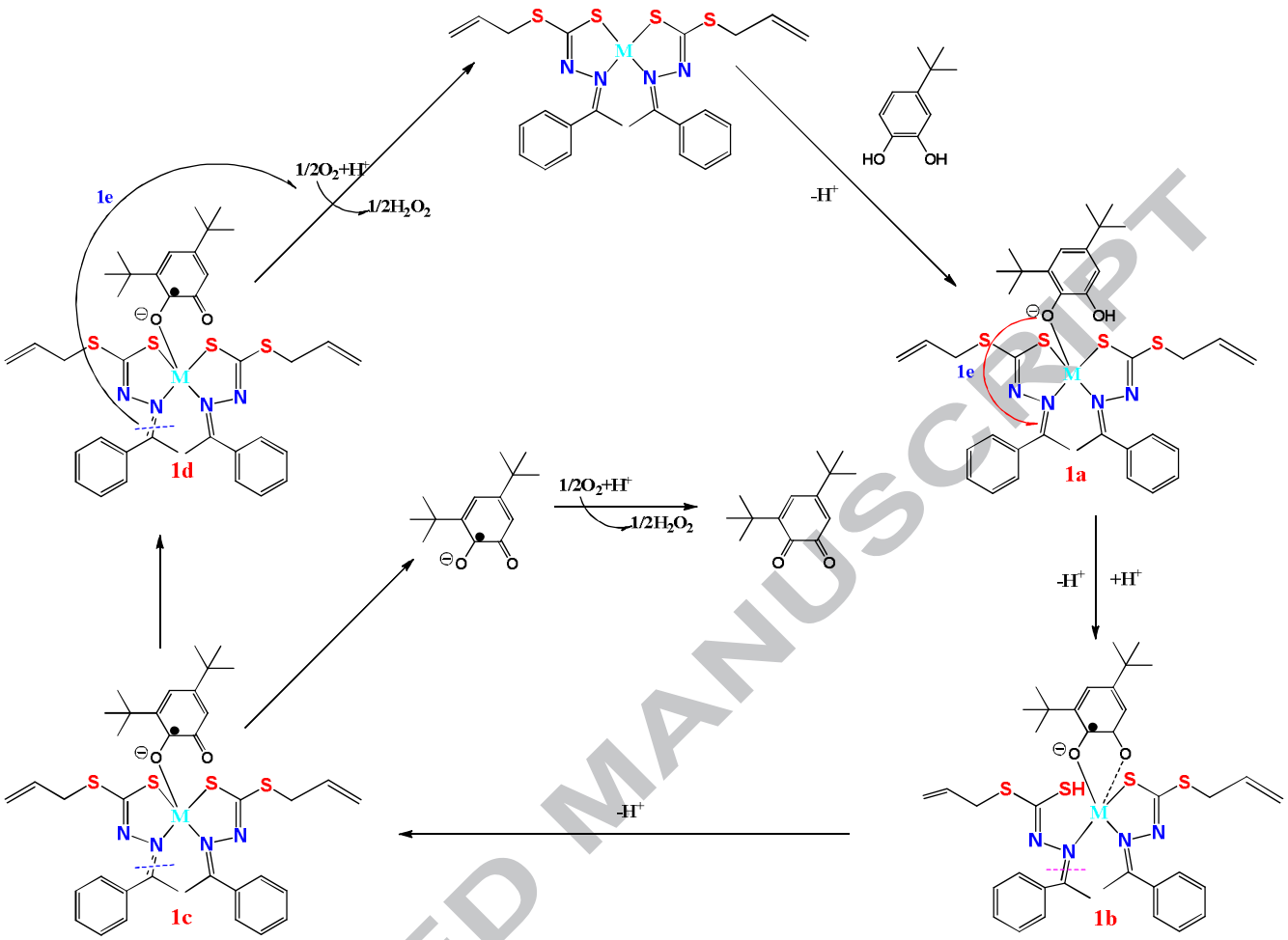

Scheme 4 Probable catalytic cycle for the oxidation of 3,5-DTBC by the square planar complexes **1**-**3**.

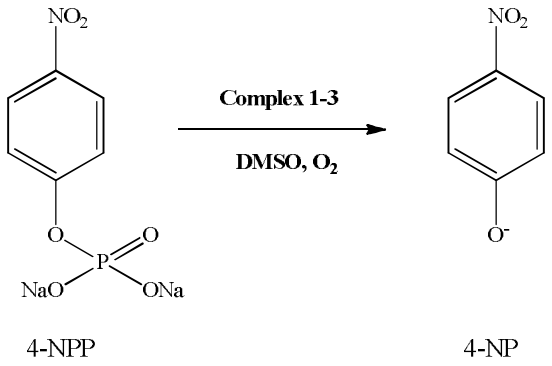

Scheme 5 Phosphatase catalytic hydrolysis of complexes **1**-**3**.

Graphical Abstract pictogram for:

Distorted tetrahedral bis-(N,S) bidentate Schiff base complexes of Ni(II), Cu(II) and Zn(II): Synthesis, characterization and biological studies

Nanjan Nanjundan[a], Ramaswamy Narayanasamy*[a], Steven Geib[b], Krishnaswamy Velmurugan[c], Raju Nandhakumar[c], Manickam Dakshinamoorthi Balakumaran[d], Pudupalayam Thangavelu Kalaichelvan[d],

[a]*Department of Chemistry, Coimbatore Institute of Technology ,Coimbatore-641 014, India.*

[b]*Department of Chemistry, University of Pittsburgh, PA 15260 USA.*

[c]*Department of Chemistry, Karunya University, Karunya Nagar, Coimbatore - 641 114, India.*

[d]*Centre for Advanced Studies in Botany, School of Life Sciences, University of Madras, Guindy Campus, Chennai - 600 025, Tamil Nadu, India.*

.

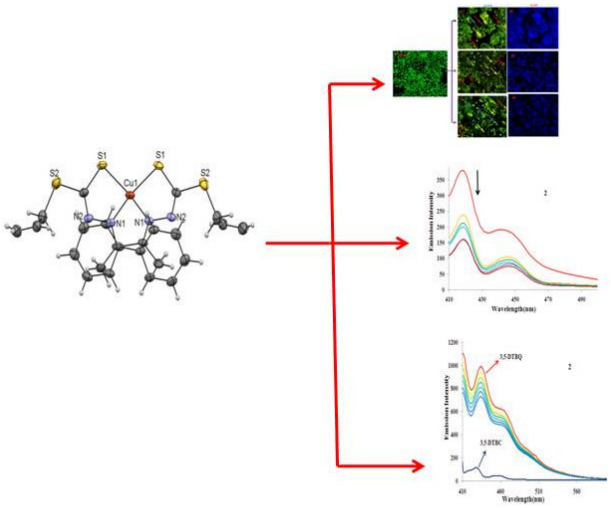

Graphical Abstract synopsis for:

Distorted tetrahedral bis-(N,S) bidentate Schiff base complexes of Ni(II), Cu(II) and Zn(II): Synthesis, characterization and biological studies

Nanjan Nanjundan[a], Ramaswamy Narayanasamy*[a], Steven Geib[b], Krishnaswamy Velmurugan[c], Raju Nandhakumar[c], Manickam Dakshinamoorthi Balakumaran[d], Pudupalayam Thangavelu Kalaichelvan[d],

[a]*Department of Chemistry, Coimbatore Institute of Technology, Coimbatore-641 014, India.*
[b]*Department of Chemistry, University of Pittsburgh, PA 15260 USA.*
[c]*Department of Chemistry, Karunya University, Karunya Nagar, Coimbatore - 641 114, India.*
[d]*Centre for Advanced Studies in Botany, School of Life Sciences, University of Madras, Guindy Campus, Chennai - 600 025, Tamil Nadu, India.*

We report here distorted tetrahedral bis-(N,S) bidentate dithiocarbazate Schiff base complexes of Ni(II), Cu(II) and Zn(II), together with their DFT and biological applications, such as catecholase/phosphatase activities, DNA/BSA interaction and *in vitro* anticancer properties.